An alternative SPH formulation: ADER-WENO-SPH

An alternative SPH formulation: ADER-WENO-SPH

Diego Avesani[a], Michael Dumbser[b], Renato Vacondio[c], Maurizio Righetti[a]

[a] *Faculty of Sciences and Technologies, University of Bozen - Bolzano, Piazza Università - Universitätsplatz 5, 39100 Bolzano-Bozen, Italy*
[b] *Department of Civil, Environmental and Mechanical engineering, University of Trento, via Mesiano 77, 38123 Trento, Italy*
[c] *Dipartimento di Ingegneria e Architettura, Università degli studi di Parma, via Università 12, 43121 Parma, Italy*

Abstract

We present a new class of fully-discrete one-step SPH schemes based on a mesh-free ADER (Arbitrary DERivatives in space and time) reconstruction on moving particles in multiple space dimensions. In particular, the new SPH scheme computes mesh-free and local high order accurate polynomials in space and time to evaluate numerical fluxes at the midpoint between two interaction particles with a proper Riemann solver within the general SPH framework of Vila (1999) for nonlinear systems of hyperbolic conservation laws. The new scheme has been carefully tested against reference solutions for both the compressible Euler and the magneto-hydrodynamics (MHD) equations. The capability of the proposed scheme to accurately capture shocks and rarefaction waves for 1D and 2D problems with minimal amount of diffusion has been demonstrated. Via numerical evidence it has been shown that the new fully-discrete one-step ADER-WENO-SPH method is computationally more efficient than WENO-SPH schemes based on classical Runge-Kutta time-stepping. This is mainly due to the fact that with ADER timestepping the expensive stencil and neighbor search needs to be done only once per time step, while with Runge-Kutta time integrators the neighbor and stencil search is needed in each Runge-Kutta stage again.

Keywords: smooth particle hydrodynamics (SPH), WENO reconstruction, fully-discrete one-step ADER schemes, meshfree Lagrangian particle method, compressible Euler equations of gasdynamics, magnetohydrodynamics

1. Introduction

SPH represents a promising numerical method, especially due to its truly mesh-free Lagrangian nature, its Galilean invariance and the intrinsic conservation of mass, linear and angular momentum. However, the scientific community working on SPH has recognized also some important limitations in SPH. For example, in its original formulation by Gingold and Monaghan (1977), SPH suffers from a lack of zeroth order consistency and several numerical instabilities which require special cures and fixes, such as the so-called tensile instability or the need for artificial viscosity in the presence of shock waves (Gui-rong and Moubin, 2003; Violeau and Fonty, 2019). At the continuous level and supposing exact integration, the spatial interpolation of SPH is actually consistent; but when the discrete spatial interpolation and the discrete quadrature are introduced, then the consistency depends on the chosen smoothing length of the kernel (the size of its compact support) and on the isotropy of the spatial particle distribution (Violeau and Fonty, 2019). To overcome these issues different ways of correcting (or re-normalizing) the kernel function have been proposed, see Liu et al. (1995); Randles and Libersky (1996); Chen et al. (1999); Liu and Liu (2006); Sibilla (2015), which aim at increasing the order of accuracy of the spatial SPH interpolation. However, those corrections have as main drawbacks the breaking of conservation of linear and/or angular momentum and they are computationally expensive, so they are rarely applied in practice.

At this point we would like to note that the aforementioned consistency problems of SPH can be avoided in the context of mesh-based Lagrangian finite volume and finite element schemes where the mesh is regenerated in each time step again around some moving generator points similar to the SPH particles. Such methods exist both in the context of finite elements, the so-called particle finite element method introduced in Idelsohn et al. (2004); Pin et al. (2007); Oñate et al. (2008); Larese et al. (2008); Idelsohn et al. (2009); Oñate et al. (2011), and in the context of direct Arbitrary-Lagrangian-Eulerian (ALE) finite volume schemes with topology changes, see e.g. Springel (2010); Gaburro et al. (2020). However, in all these approaches the entire mesh needs to be regenerated at each time step again,

which is a clear disadvantage compared to SPH. Alternatively, in the intent to exploit ALE mesh based schemes in the SPH framework, Lind and Stansby (2016) have derived the so called Incompressible Smoothed Particle Hydrodynamics (ISPH) method, which combines high-order smoothing kernels over regular distributed and not moving particles, thus renouncing the Lagrangian description of the motion.

Moving to the SPH context and its improvements, some authors have introduced a diffusion term in the continuity equation, see Ferrari et al. (2009); Molteni and Colagrossi (2009); Antuono et al. (2010); Marrone et al. (2011); Green et al. (2019); Sun et al. (2017), which improves the robustness and the accuracy of the scheme when simulating free surface flows of weakly compressible fluids. Another way that has become quite popular is the so-called shifting technique, see Xu et al. (2009); Lind et al. (2012); Oger et al. (2016a); Sun et al. (2017); McLoone and Quinlan (2020), which consists in introducing a correction to the particle velocity in the Lagrangian particle motion. In this context, it is worth to mention Oger et al. (2016b)'s work, which has introduced a new formulation of the corrected velocity within an Arbitrary Lagrangian Eulerian formalism.

A mathematically rigorous and provably stable SPH formalism has been introduced for the first time by Vila (1999); Ben Moussa et al. (1999); Ben Moussa (2006), based on a meshless Lagrangian finite volume-type formulation and where Riemann solvers are used between each pair of interacting particles. The main advantage of this formulation is that stability is achieved without introducing any artificial viscosity parameter but treating each particle particle interaction as a one dimensional Riemann problem. The same algorithm was then applied to free-surface impacts (Oger et al., 2016c) fluid-structure interaction problems (Fourey et al., 2017), turbine simulations (Phoevos et al., 2012; Marongiu et al., 2010) and wave impact on structures (Rogers et al., 2010; Pourya et al., 2012, 2013). Nevertheless, this SPH scheme results to be excessively diffusive even when applying Gudonov's flux based on the exact Riemann solver. Motivated by the results obtained in the above references, an extension of the Vila and Ben Moussa approach to better than second order meshfree Moving Least-Squares (MLS) WENO reconstruction was derived in Avesani et al. (2014) and subsequently applied to anisotropic dispersion in porous media in Avesani et al. (2015, 2017). Starting from this new MLS-WENO approach, (Nogueira et al., 2016) present a new SPH scheme based on Moving Least Squares reconstructions in combination with *a posteriori* Multi-dimensional Optimal Order Detection (MOOD), see Clain et al. (2011); Diot et al. (2012, 2013), which results in an efficient, stable and little-dissipative SPH scheme. It is worth to mention that, another approach able to achieve meshfree high order reconstruction has been recently presented in (King et al., 2020), where a novel framework for local and high order difference operators for arbitrary node distribution is presented and apply for the numerical solution of PDEs.

The high order spatial MLS reconstruction is able to improve the accuracy of the standard SPH interpolation, recovering high-order spatial convergence also for random particle distribution. However, in Avesani et al. (2014) the time integration scheme was achieved by adopting a third order TVD Runge-Kutta scheme. This means that the SPH-WENO procedure had to be repeated for each Runge-Kutta substage, leading to significant computational cost in comparison with the standard ALE-SPH scheme proposed in Vila (1999); Ben Moussa et al. (1999). To overcome this issue in this paper a new mesh-free ADER approach (Arbitrary DERivative in space and time) is adopted to guarantee a high order space-time reconstruction. The novel idea is hence to define around each particle high order polynomials in both space and time, and consequently computing the SPH summation for each particle only once for each time step. The resulting fully-discrete one-step ADER-WENO-SPH algorithm is obtained by means of the following steps: i) Moving-Least Squares WENO reconstruction; ii) local time evolution of the spatial reconstruction polynomials via a weak formulation of the governing PDE system in space-time; iii) update of the conservative quantities via the exact or approximate solution of Riemann problems between each pair of particles i and j.

The ADER approach goes back to the pioneering work of Toro and Titarev, who developed this method as an extension of Godunov's first order scheme to finite volume schemes of arbitrary high order of accuracy both in space and time, see Titarev and Toro (2002); Toro and Titarev (2002); Titarev and Toro (2005); Toro and Titarev (2006). The underlying idea of the ADER method is the approximate solution of a generalized Riemann problem (GRP), where initial data are given by piecewise polynomials, separated by a discontinuity. This corresponds to the natural data representation in high-order finite volume and discontinuous Galerkin (DG) finite element schemes. Later, ADER schemes were also extended to finite volume schemes on unstructured meshes, to space-time adaptive Cartesian grids (AMR) and to the discontinuous Galerkin finite element framework, see Dumbser et al. (2007, 2008b); Boscheri and Dumbser (2013, 2014); Boscheri et al. (2014); Dumbser et al. (2013, 2008a); Boscheri and Dumbser (2017).

This paper is organized as follows: Section 2 first briefly describes the Vila and Ben-Moussa SPH approach based on Riemann solvers and then introduces the new meshfree ADER reconstruction giving all details on the spatial

WENO reconstruction procedure and on the local space-time predictor. In section 3 some numerical examples are presented and the new scheme is compared with existing standard SPH methods. The paper is rounded-off with some closing remarks and an outlook to future work in section 4.

2. Numerical scheme

This paper considers nonlinear homogeneous systems of conservation laws of the form

$$\frac{\partial \mathbf{q}}{\partial t} + \nabla \cdot \mathbf{F}(\mathbf{q}) = 0 \tag{1}$$

in the domain $\Omega \in \mathbb{R}^2$, where $\mathbf{q}$ is the vector of conserved variables; $\mathbf{F}(\mathbf{q})$ is the flux tensor; $\mathbf{x} = (x, y)$ is the vector of spatial coordinates and t is the time variable. Specifically, $\mathbf{q}$ is defined in the set of admissible states Ω_q; and $\mathbf{F}(\mathbf{q})$ reads as $\mathbf{F}(\mathbf{q}) = (\mathbf{f}(\mathbf{q}), \mathbf{g}(\mathbf{q}))$, where $\mathbf{f}$ and $\mathbf{g}$ are the fluxes along the x and y directions, respectively.

Following the general approach of Vila and Ben Moussa, the computational domain Ω is discretized by a finite set of N_p particles $\mathcal{P}_i$ with position $\mathbf{r}_i$ and associated volume V_i. A semi-discrete scheme for the approximation of Equation (1) reads then as follows:

$$\frac{d}{dt} V_i \mathbf{q}_i = -\sum_{j=1}^{N} V_i V_j 2 \left(\mathbf{G}_{ij} - \mathbf{H}_i \right) \cdot \nabla W_{ij}, \tag{2}$$

$$\frac{d}{dt} V_i = \sum_{j=1}^{N} \left(\bar{\mathbf{v}}_{ij} - \mathbf{v}_i \right) \cdot \nabla W_{ij}, \tag{3}$$

$$\frac{d}{dt} \mathbf{r}_i = \mathbf{v}_i. \tag{4}$$

Here, Equation (2) represents the numerical integration of Equation (1) in the Lagrangian framework; Equation (3) considers the evolution of the particle volumes due to the motion of the particles; Equation (4) describes the evolution of the position $\mathbf{r}_i = (x_i, y_i)$ of each Lagrangian particle which changes in time according to the particle velocity $\mathbf{v}_i$. The term $\mathbf{q}_i$ represents the discrete numerical solution for the state vector $\mathbf{q}$ associated with each particle; $\mathbf{G}_{ij}$ is the numerical flux tensor; $\bar{\mathbf{v}}_{ij}$ is the velocity at the interface between two interacting particles $\mathcal{P}_i$ and $\mathcal{P}_j$; $\mathbf{H}_i$ is the additional Lagrangian flux tensor computed at the state of the *i-th*; W_{ij}, is the so called smoothing kernel function centered in $\mathbf{r}_i$ and evaluated in $\mathbf{r}_j$ and which is typical of the SPH formalism; its gradient is denoted by ∇W_{ij}, where the derivative is computed with respect to $\mathbf{r}_j$. Using for example the cubic B-spline function (Monaghan, 2005), W_{ij} reads as:

$$W_{ij} = \frac{\kappa}{h_{ij}^d} \begin{cases} 1/3 - q_{ij}^2 + q_{ij}^3/2, & \text{if } 0 \le q_{ij} < 1, \\ (2 - q_{ij})^2 + q_{ij}^3, & \text{if } 1 \le q_{ij} \le 2, \\ 0, & \text{if } q_{ij} > 0, \end{cases} \tag{5}$$

where $q_{ij} = \left\| \mathbf{r}_j - \mathbf{r}_i \right\| / h_{ij}$; κ is a normalization constant so that $\int_{\mathbb{R}^d} W dV = 1$; d is the number of space dimensions, i.e. $d = 2$ in our applications; and h_{ij} is the so called smoothing length (Monaghan, 1994, 2005), which is either chosen as a global constant throughout the computational domain, or is locally adjusted to the particle density as

$$h_{ij} = \frac{1}{2} \left(h_i + h_j \right), \qquad \text{with} \qquad h_i = \sigma \sqrt[d]{V_j}, \tag{6}$$

with d the number of space dimensions and σ a scaling factor.

As it can be noticed, $\mathbf{G}_{ij}$ is the key feature of the Vila and Ben Moussa's SPH scheme and at the same time it constitutes the main difference with respect to the standard SPH method. The term $\mathbf{G}_{ij}$ is a *numerical flux* between two particles $\mathcal{P}_i$ and $\mathcal{P}_j$ and describes the interaction between the discrete volumes V_i and V_j along the direction $\mathbf{n}_{ij}$ connecting the particles $\mathcal{P}_i$ and $\mathcal{P}_j$ using a Lagrangian Finite Volume formulation. The numerical flux $\mathbf{G}_{ij}$ is computed

at the aid of exact or approximate Riemann solvers in a co-moving frame. When using the Godunov flux Godunov (1959) based on the exact Riemann solver Toro (1997), it reads as follows:

$$\mathbf{G}_{ij} = \mathbf{G}_{ij}(\mathbf{q}_i, \mathbf{q}_j) = \mathbf{F}_{ij}(\mathbf{q}_E) - \mathbf{q}_E \otimes \mathbf{v}_{ij}, \tag{7}$$

where $\mathbf{q}_i$ and $\mathbf{q}_j$ are the state variables of the two interacting particles, $\mathbf{q}_E = \mathbf{q}_E(\mathbf{q}_i, \mathbf{q}_j)$ is the so-called Godunov state that results from the solution of the Riemann problem between these two states and $\mathbf{v}_{ij}$ is the particle velocity at the midpoint $\bar{\mathbf{r}}_{ij} = \frac{1}{2}(\mathbf{r}_i + \mathbf{r}_j)$, which is also computed by the Riemann solver. $\mathbf{F}_{ij}(\mathbf{q}_E)$ is the flux tensor evaluated in the Godunov state. It is worth to be noticed that the SPH approach of Vila (1999) uses the values $\mathbf{q}_i$ and $\mathbf{q}_j$ of the two interacting particles in order to solve the Riemann problem, which consequently leads to a first order scheme that is affected by very high numerical diffusion, as already shown in Avesani et al. (2014).

In order to overcome these drawbacks, Avesani et al. (2014) introduce the so called MLS-WENO-SPH formulation, where the numerical fluxes, as well the interface velocity, are evaluated at the particle interfaces using high order mesh-free WENO reconstruction polynomials. The MLS-WENO-SPH scheme performs a piecewise high order accurate essentially non-oscillatory WENO reconstruction $\mathbf{w}_i(\mathbf{x})$ around each particle's position $\mathbf{r}_i$, knowing the point values $\mathbf{q}_j$ of particles in its surrounding. Then, the local Riemann problem between the two interacting particles $\mathcal{P}_i$ and $\mathcal{P}_j$ is solved at the midpoint $\bar{\mathbf{r}}_{ij} = \frac{1}{2}(\mathbf{r}_i + \mathbf{r}_j)$ using the local high order WENO reconstruction polynomials $\mathbf{w}_i(\mathbf{x})$ and $\mathbf{w}_j(\mathbf{x})$, which allows to extrapolate the left state $\mathbf{q}_{ij}^- = \mathbf{w}_i(\bar{\mathbf{r}}_{ij})$ and the right state $\mathbf{q}_{ij}^+ = \mathbf{w}_j(\bar{\mathbf{r}}_{ij})$ at the moving particle interfaces. Using for example the Rusanov flux, see Rusanov (1961), as used in Avesani et al. (2014) and also applied for the rest of this paper, Equation (7) reduces to:

$$\mathbf{G}_{ij} = \frac{1}{2}\left(\mathbf{H}\left(\mathbf{q}_{ij}^+, \bar{\mathbf{v}}_{ij}\right) + \mathbf{H}\left(\mathbf{q}_{ij}^-, \bar{\mathbf{v}}_{ij}\right)\right) - \frac{c_{ij}}{2}\left(\mathbf{q}_{ij}^+ - \mathbf{q}_{ij}^-\right) \otimes \mathbf{n}_{ij}, \tag{8}$$

with

$$\bar{\mathbf{v}}_{ij} = \frac{1}{2}(\mathbf{v}_{ij}^- + \mathbf{v}_{ij}^+), \tag{9}$$

where $\mathbf{H}$ is the flux tensor of in the reference frame moving with velocity $\mathbf{v}$, which reads as:

$$\mathbf{H}(\mathbf{q}, \mathbf{v}) = \mathbf{F}(\mathbf{q}) - \mathbf{q} \otimes \mathbf{v}. \tag{10}$$

The term c_{ij} is instead the maximum absolute value of the eigenvalues of the Jacobian matrix $\mathbf{A_n} = \mathbf{A_n}(\mathbf{q}, \mathbf{v}) = \partial\mathbf{H}/\partial\mathbf{Q} \cdot \mathbf{n}_{ij}$, evaluated along the direction $\mathbf{n}_{ij}$ in a moving frame, which reads as:

$$c_{ij} = \max(|\mathbf{\Lambda}_i^-|, |\mathbf{\Lambda}_j^+|), \tag{11}$$

with $\mathbf{\Lambda}$ being the diagonal matrix of eigenvalues of $\mathbf{A_n}(\mathbf{q}, \mathbf{v})$. For the use of other approximate Riemann solvers in the context of SPH schemes, see Rossi et al. (2017).

Despite the advantages of the MLS-WENO-SPH method in terms of higher accuracy and less numerical dissipation, it results to be computationally rather expensive. Using for example a third order TVD Runge-Kutta scheme for the time integration of the system (2-4) it results that the SPH summations as well the MLS-WENO reconstruction have to be performed once per Runge-Kutta stage and thus three times for each time step, making the algorithm rather expensive. In the rest of this paper we will refer to the MLS-WENO-SPH scheme with Runge-Kutta time discretization as RK-WENO-SPH.

In order to overcome this drawback in the RK-WENO-SPH scheme and simultaneously exploit its accuracy, we propose an alternative procedure in order to compute high-order local mesh-free reconstruction polynomials not only in space, as in the original RK-WENO-SPH formulation, but also in time. In particular, the space-time reconstruction approach presented here is based on the so called ADER schemes, usually used in the context of mesh based methods and hereafter extended to the meshfree framework for the first time.

The reconstruction polynomials, the particle search algorithm and the SPH summation are computed thus only once for each time step, in contrast to the original RK-WENO-SPH formulation with Runge-Kutta time integration. Hence, the key idea presented in this paper is to evolve the spatial MLS-WENO reconstruction polynomials locally in time in order to compute the high order polynomials in both space and time, which then allow to evaluate the numerical fluxes at the midpoint between two interaction particles at high accuracy. The temporal evolution of the

spatial reconstruction polynomials provides a so-called predictor solution (evolution of the PDE in the small), since it neglects the contribution of the fluxes from neighboring particles, which are then taken into account later in a corrector step based on the Vila SPH framework, in order to evolve the discrete solution in time. This approach is similar to the procedure used in the MUSCL-Hancock scheme, see van Leer (1979); Toro (1997), and in the original ENO scheme of Harten et al. (1987).

In the following, we summarize the main steps of the MLS-WENO reconstruction (Avesani et al., 2014, 2015, 2017), and we introduce the new mesh-free local ADER reconstruction in space-time.

2.1. MLS-WENO reconstruction

The adopted MLS-WENO framework is not based on kernel functions, as in the Dilts (1999)'s formulation, but produces essentially non-oscillatory local Taylor series reconstructions computed according three main steps: local stencils set-up; Moving-Least-Squares interpolation on each local stencil; and non linear weighted combination of the local Taylor series functions.

The first step, knowing the particle positions $\mathbf{r}_i$ at computational time t^n, is to construct the so called central stencil $\mathcal{S}_0^i$ and the sectorial stencils $\mathcal{S}_s^i$ (see Dumbser and Käser (2007)), with $s \in [1, 8]$, for each particle as:

$$\mathcal{S}_0^i = \bigcup_k^{ne_0} \mathcal{P}_{j(k)}, \qquad \left\|\mathbf{r}_{ij}\right\| \leq h_{i,mls}; \tag{12a}$$

$$\mathcal{S}_s^i = \bigcup_k^{ne_s} \mathcal{P}_{j(k)}, \quad \left\|\mathbf{r}_{ij}\right\| \leq 2h_{i,mls} \quad \text{and} \quad \theta \in [(s-1)\pi/4, s\pi/4]; \tag{12b}$$

where $h_{i,mls}$ is a characteristic length scale and θ is the angle computed as $\tan(\theta) = \frac{y_{ji}}{x_{ji}}$, with y_{ji}, x_{ji} the Cartesian coordinates of the vector $\mathbf{r}_{ij} = \mathbf{r}_j - \mathbf{r}_i$ connecting the particles $\mathcal{P}_i$ and $\mathcal{P}_j$. Furthermore, k (with $1 \leq k \leq ne_s$) represents a local index counting the particles $\mathcal{P}_j$ in the stencil; $j = j(k)$ is the mapping from the local index k to the global particle number i; and ne_s is the total number of particles in the stencil itself.

For each of the nine reconstruction stencils a moving least-squares (MLS) reconstruction polynomials of the conservative variables is computed as:

$$\mathbf{w}_i^s(\mathbf{x}, t^n) = \mathbf{q}_i^n + \sum_{m=1}^{nc-1} \hat{\mathbf{w}}_{m,s}^n \phi_m(\boldsymbol{\xi}); \tag{13}$$

where, $\boldsymbol{\xi} = \boldsymbol{\xi}(\mathbf{x})$ are normalized reference coordinates, which in two dimensions read

$$\boldsymbol{\xi} = \begin{pmatrix} \xi \\ \eta \end{pmatrix} = \frac{1}{h_{i,mls}} \begin{pmatrix} x - x_i \\ y - y_i \end{pmatrix}; \tag{14}$$

and $\hat{\mathbf{w}}_{m,s}^n$ are the coefficients of the reconstruction polynomial of the *s-th* stencil. The basis functions $\phi_m(\boldsymbol{\xi})$ are chosen to be simple, rescaled Taylor monomials and are defined as follows:

$$\phi_m(\xi, \eta) = \frac{\xi^a \eta^b}{h_{mls}^{(a+b)}}, \tag{15}$$

where $a + b = l$, and l ranges from 1 to M (Zwillinger, 2003; Agossler Albert, 2001), with M the maximum degree of the reconstruction polynomial (13). The term $n_c - 1$ is the number of unknown expansion coefficients in each of the nine polynomials and in two dimension is equal to

$$n_c = \frac{(M+1)(M+2)}{2}. \tag{16}$$

It follows that Equation (13) represents nine rescaled Taylor series expansions of order M around $\mathbf{r}_i$, where $\hat{\mathbf{w}}_{m,s}^n$ are the unknown expansion coefficients that can be computed for each stencil requiring $\mathbf{w}_i^s(\mathbf{r}_j, t^n) = \mathbf{q}_j^n$, leading to the following set of equations for each stencil:

$$\mathbf{q}_j^n - \mathbf{q}_i^n = \sum_{m=1}^{nc-1} \hat{\mathbf{w}}_{m,s}^n \phi_m(\boldsymbol{\xi}_j), \quad \forall \mathcal{P}_j \in S_s^i. \tag{17}$$

According to Avesani et al. (2014), n_{es}, which is the number of particles in each stencil and consequently the number of equations in the linear system (17), has to satisfy $n_{es} > n_c$. Therefore Equation (17) becomes an overdetermined linear algebraic system, which can be solved by a classical least-squares minimization. Since the particles are also moving, this reconstruction is called a Moving-Least-Squares (MLS) reconstruction. Finally, in order to reduce spurious oscillations at shock waves, the essentially non-oscillatory spatial reconstruction polynomial $\mathbf{w}_i(\mathbf{x}, t^n)$ for particle $\mathcal{P}_i$ is obtained by a non-linear WENO combination of the polynomials $\mathbf{w}_i^s(\mathbf{x}, t^n)$ of all stencils, see Jiang and Shu (1996):

$$\mathbf{w}_i(\mathbf{x}, t^n) = \sum_{s=0}^{ns-1} \omega_s \mathbf{w}_i^s(\mathbf{x}, t^n), \tag{18}$$

where ω_s are the normalized nonlinear weights, which are defined as

$$\omega_s = \frac{\widetilde{\omega}_s}{\sum_{r=1}^{ns} \widetilde{\omega}_r}, \tag{19}$$

with the non-normalized weights $\widetilde{\omega}_s$ that assume the following form, see (Dumbser et al., 2008a,b):

$$\widetilde{\omega}_s = \frac{\lambda_s}{(\epsilon + \sigma_s)^r}. \tag{20}$$

Throughout this paper the constants ϵ and r are set equal to 10^{-14} and 4, respectively, while λ_s are the linear weights with $\lambda_0 = 10^5$ for the central the stencil and $\lambda_s = 1$ for the one-sided sectorial stencils ($1 \leq s \leq 8$). As in (Avesani et al., 2014, 2015), the smoothness indicator is simply computed as follows:

$$\sigma_s = \sum_{1 \leq |m| \leq M} \left(\hat{\mathbf{w}}_{m,s}^n \right)^2. \tag{21}$$

For the sake of clarity, Figure (1) summarizes the key features of the MLS-WENO scheme. In particular, Figure (1a) shows the central stencils for two generic interacting particles $\mathcal{P}_i$ and $\mathcal{P}_j$; Figure (1b) shows the central and lateral stencils for a particle $\mathcal{P}_i$; Figure (1c) the WENO reconstruction polynomials of particle $\mathcal{P}_i$ for the central stencil $\mathcal{S}_0^i$ and for the lateral stencils $\mathcal{S}_1^i$ and $\mathcal{S}_4^i$ respectively. Finally, Figure (1d) illustrates the time integration according the third order TVD scheme of reconstruction polynomial of two generic interacting particles and consequently the requirement to apply the MLS-WENO reconstructions at each time step. It has also to point it out that the smoothing length in the kernel interpolation $h_{i,mls}$ is variable for each particle and its function of particle volume, which reads as:

$$h_{i,mls} = \sqrt[v]{V_i}. \tag{22}$$

Each particle, at the end of MLS-WENO reconstruction, is thus characterized by a local reconstruction polynomial obtained by a non-linear combination of the nine polynomials each of them reconstructed on one different stencil according to the Equation (13).

At this point we would like to note two aspects of the above mention MLS-WENO reconstruction. Firstly, an alternative WENO reconstruction technique could also be adopted here, which is the well-known central WENO (CWENO) reconstruction of Puppo, Russo and Semplice et al., see Levy et al. (1999, 2000); Cravero et al. (2018); Semplice et al. (2016); Dumbser et al. (2017). Secondly, MLS-WENO can be directly generalized to 3D as long as we consider 3D stencils as well as 3D reconstruction polynomials.

2.2. Local space-time predictor

Due to the MLS-WENO reconstruction in space, the numerical solution at time t^n is not only represented by the discrete values $\mathbf{q}_i^n$ on each particle, but also by the interpolation polynomials $\mathbf{w}_i(\mathbf{x}, t^n)$, one for each particle. Hence, the main idea of this paper is now to evolve these interpolation polynomials locally in time in order to obtain *space-time* polynomials, which will subsequently be employed for integrating the numerical fluxes in time. The local evolution (predictor step) is performed based on the ADER approach, which has already been successfully applied to the Finite-Volume framework and which is here extended to meshfree Lagrangian particle methods for the first time.

In order to move into the ADER framework, it is mandatory to represent the numerical solution for each particle in a square element $\mathcal{R}_i$ at time t^n starting from the spatial WENO reconstruction polynomials $\mathbf{w}_i(\mathbf{x}, t^n)$. The first step is to define the element $\mathcal{R}_i$ as $[x_i - l_{mls,i}; x_i + l_{mls,i}] \times [y_i - l_{mls,i}; y_i + l_{mls,i}]$ and which is represented in Figure (2a) for the sake of clarity. In addition, also the spatial WENO reconstruction polynomial is rewritten as

$$\mathbf{u}_i(\mathbf{x}, t^n) = \sum_{l=1}^{\mathcal{N}} \psi(\mathbf{x}) \hat{\mathbf{u}}_{i,l}^n \quad \mathbf{x} \in \mathcal{R}_i; \tag{23}$$

where $\psi(\mathbf{x})$ are spatial basis functions; $\hat{\mathbf{u}}_{i,l}^n$ are the expansion coefficients computed at simulation time t^n; and $\mathbf{x} = (x, y)$ are the Cartesian coordinates. In Equation (23) $\psi(\mathbf{x})$ are chosen as tensor-products of Lagrange interpolation polynomials of degree M which pass through the tensor-product of $(M+1)^d$ Gauss-Legendre quadrature points, where d is the number of space dimensions. The term $\mathcal{N}$ is the number of expansion coefficients and is given by:

$$\mathcal{N} = \frac{1}{d!} \prod_{m=1}^{d} (M + m) \tag{24}$$

We underline that, in order to simplify the notation, the classical tensor index notation based on the Einstein summation convention is used for the rest of the paper. This implies that the coefficients $\hat{\mathbf{u}}_{i,l}^n$ are the values of the conservative variables computed in the Gauss-Legendre quadrature points using the spatial WENO interpolation polynomial $\mathbf{w}_i(\mathbf{x}, t^n)$. For the sake of clarity, Figures (2a) and (2b) show the Gauss-Legendre quadrature points for $M = 2$ and the coefficients computed according to Equation (23) for the two dimensional case.

The second step consists in evolving in time and locally the space polynomial (23) in the space-time control volume $\tilde{\mathcal{R}}_i = \mathcal{R}_i \times [t^n, t^{n+1}]$. In particular, following Continuous and Discontinuous Galerkin methods (Ern and Guermond, 2004; Bassi et al., 2012), it is possible to write Equation (1) in the so called weak formulation, which reads as:

$$\int_{t^n}^{t^{n+1}} \int_{\mathcal{R}(t)_i} \theta_k \frac{\partial \mathbf{q}}{\partial t} dt d\mathbf{x} + \int_{t^n}^{t^{n+1}} \int_{\mathcal{R}(t)_i} \theta_k \nabla \cdot \mathbf{F}(\mathbf{q}) dt d\mathbf{x}, \tag{25}$$

where $\theta_k = \theta_k(\mathbf{x}, t)$ are a set of space-time test functions of maximum degree M.

Given the weak formulation of the PDE in both space and time depict in Equation (25), it is possible to introducing a reference element $\tilde{\mathcal{R}}_E = [0, 1]^d \times [0, 1]$ and a linear mapping with $\tilde{\mathcal{R}}_i$. This establishes the preliminary step in order to move to the Lagrangian version of the local space-time Galerkin methods, introduced in (Boscheri and Dumbser, 2013) in the moving meshes framework and hereafter extended in the SPH schemes. In particular, the adoption of moving local space-time continuous-Galerkin predictor emerges to be mandatory due to the motion of the particles which deformate the control volume $\tilde{\mathcal{R}}_i$ and does not allow the use of a linear mapping.

Consequently, we introduce $\tilde{\mathbf{x}} = (x, y, t)$ as physical space-time coordinate vector and $\tilde{\boldsymbol{\xi}} = (\xi, \eta, \tau)$ as the reference space-time coordinate vector while $\boldsymbol{\xi} = (\xi, \eta)$ are the purely spatial coordinates of the reference element. Similarly, the use of a proper isoparametric mapping allows to transform the physical space-time element to the unit reference space-time element. Figures (2c-2d) illustrates this mapping and respectively the space-time and the unit reference space-time elements. In addition, the Jacobian matrix of the transformation reads:

$$\boldsymbol{J}_{st} = \frac{\partial \tilde{\mathbf{x}}}{\partial \tilde{\xi}} = \begin{pmatrix} x_\xi & x_\eta & x_\tau \\ y_\xi & y_\eta & y_\tau \\ 0 & 0 & \Delta t \end{pmatrix}, \tag{26}$$

while its inverse is given by

$$\boldsymbol{J}_{st}^{-1} = \frac{\partial \tilde{\xi}}{\partial \tilde{\mathbf{x}}} = \begin{pmatrix} \xi_x & \xi_y & \xi_t \\ \eta_x & \eta_y & \eta_t \\ 0 & 0 & \frac{1}{\Delta t} \end{pmatrix}. \tag{27}$$

Using the reference space-time element and the inverse Jacobian matrix (27) of the isoparametric mapping between the reference and physical element, it is possible to write equation (25) in terms of reference coordinates $\boldsymbol{\xi}$ and τ as

$$\int_0^1 \int_{\mathcal{R}_E} \theta_k \frac{\partial \mathbf{q}}{\partial \tau} d\tau d\boldsymbol{\xi} + \int_0^1 \int_{\mathcal{R}_E} \theta_k \left(\mathbf{H}^*(\mathbf{q}) + \nabla_\xi \cdot \mathbf{F}^*(\mathbf{q}) \right) d\tau d\boldsymbol{\xi}. \tag{28}$$

We point out that ∇_ξ and $\mathbf{F}^*$ have been introduced in order to consider properly the change of variables and are defined as:

$$\nabla_\xi = \begin{pmatrix} \partial_\xi \\ \partial_\eta \end{pmatrix}, \qquad \nabla = \left(\frac{\partial \boldsymbol{\xi}}{\partial \mathbf{x}}\right)^T \nabla_\xi, \qquad \text{and} \qquad \mathbf{F}^* = \Delta t \left(\frac{\partial \boldsymbol{\xi}}{\partial \mathbf{x}}\right)^T \mathbf{F}. \tag{29}$$

It has to be noticed the additional term $\mathbf{H}(\mathbf{q})^*$ in Equation (28) respect to the standard weak formulation, which is defined as:

$$\mathbf{H}^*(\mathbf{q}) = \Delta t \frac{\partial \mathbf{q}}{\partial \xi} \frac{\partial \xi}{\partial t}; \tag{30}$$

and is due to the Lagrangian particle motion.

The next step represents the main difference between standard Galerkin approaches and the new families of ADER schemes introduced in (Dumbser et al., 2008b) in the Eulerian framework and successively extended to Lagrangian moving meshes in (Boscheri and Dumbser, 2013). Equation (28) is indeed integrated by parts in time and not in space as standard Galerkin schemes. The main advantage is thus to keep the information local in space where no extra-information are required. This yields to:

$$\int_{\mathcal{R}_E} \theta_k(\boldsymbol{\xi},1)\mathbf{q}d\boldsymbol{\xi} - \int_{\mathcal{R}_E} \theta_k(\boldsymbol{\xi},0)\mathbf{u}(\boldsymbol{\xi},0)d\boldsymbol{\xi} - \int_0^1 \int_{\mathcal{R}_E} \frac{\partial}{\partial \tau}\theta_k(\boldsymbol{\xi},\tau)\mathbf{q}d\boldsymbol{\xi}d\tau + \int_0^1 \int_{\mathcal{R}_E} \Big(\mathbf{H}^*(\mathbf{q}) + \nabla_\xi \cdot \mathbf{F}^*(\mathbf{q})\Big)\theta_k(\boldsymbol{\xi},\tau)d\boldsymbol{\xi}d\tau, \tag{31}$$

where, for sake of clarity, the dependency of θ_k on space and time has been made explicit. In analogy with the local spatial reconstruction expressed by Equation (23), also the space-time test function can be used in order to approximate the space-time predictor solution in the space-time reference element as

$$\mathbf{q}_i(\mathbf{x},t) = \sum_{l=1}^{\mathcal{L}} \theta_l(\tilde{\boldsymbol{\xi}})\hat{\mathbf{q}}_{l,i}^n := \theta_l \hat{\mathbf{q}}_{l,i}^n. \tag{32}$$

In a similar way also the nonlinear fluxes can be interpolated as

$$\mathbf{F}_i^*(\mathbf{x},t) = \sum_{l=1}^{\mathcal{L}} \theta_l(\tilde{\boldsymbol{\xi}})\hat{\mathbf{F}}_{l,i}^* := \theta_l \hat{\mathbf{F}}_{l,i}^*, \tag{33}$$

as well the additional Lagrangian term is written as:

$$\mathbf{H}_i^*(\mathbf{x},t) = \sum_{l=1}^{\mathcal{L}} \theta_l(\tilde{\boldsymbol{\xi}})\hat{\mathbf{H}}_{l,i}^* := \theta_l \hat{\mathbf{H}}_{l,i}^*. \tag{34}$$

Hence, substituting Equations (23), (32), (33) and (34) into (31) we obtain the following system of equations:

$$\begin{aligned}\left(\int_{\mathcal{R}_E} \theta_k(\boldsymbol{\xi},1)\theta_l(\boldsymbol{\xi},1)d\boldsymbol{\xi} - \int_0^1 \int_{\mathcal{R}_E} \frac{\partial \theta_k}{\partial \tau}\theta_l d\boldsymbol{\xi}d\tau\right)\hat{\mathbf{q}}_{i,l} &= \left(\int_{\mathcal{R}_E} \theta_k(\boldsymbol{\xi},0)\phi_l d\boldsymbol{\xi}\right)\hat{\mathbf{u}}_{i,l}^n \\ &- \left(\int_0^1 \int_{\mathcal{R}_E} \theta_k \nabla_\xi \theta_l d\boldsymbol{\xi}d\tau\right)\hat{\mathbf{F}}_{i,l}^* - \left(\int_0^1 \int_{\mathcal{R}_E} \theta_k \theta_l d\boldsymbol{\xi}d\tau\right)\hat{\mathbf{H}}_{i,l}^*,\end{aligned} \tag{35}$$

where the unknowns are the coefficients $\hat{\mathbf{q}}_{i,l}$ of the local space-time predictor solution, while the terms $\hat{\mathbf{u}}_{i,l}$ are the known coefficients of spatial reconstruction at time t^n in the element $\mathcal{R}_i$. The unknowns $\hat{\mathbf{q}}_{i,l}$ can be easily computed using a fast converging fixed-point iteration, see Dumbser et al. (2008a); Busto et al. (2020).

Since the particles are moving also the vertex coordinates motion of the local space-time element $\tilde{\mathcal{R}}_i$ has to be properly considered. In particular, as for the Equations (32), (33) and (34), it is possible use space-time test functions in order to describe the local vertex in the local element $\mathcal{R}_i$ as:

$$\mathbf{x}_i(\tilde{\boldsymbol{\xi}}) = \sum_{l=1}^{\mathcal{L}} \theta_l(\tilde{\boldsymbol{\xi}})\mathbf{x}_{i,l} \tag{36}$$

where $\mathbf{x}_{i,l}$ are the space-time coordinates of the Gauss-Lagrangian nodal point in the element $\mathcal{R}_i$. Similarly, the node velocities are approximated as:

$$\mathbf{v}_i(\tilde{\boldsymbol{\xi}}) = \sum_{l=1}^{\mathcal{L}} \theta_l(\tilde{\boldsymbol{\xi}}) \mathbf{v}_{i,l}. \tag{37}$$

Finally, Equation (4), which models the motion of the *i-th* particle, is approximated by Equation (36) and (37) and then integrated in the space-time reference element, analogously to Equation (1) in the ADER framework. This yields to:

$$\left(\int_0^1 \int_{\mathcal{R}_E} \frac{\partial \theta_k}{\partial \tau} \theta_l \right) \mathbf{v}_{i,l} = \left(\int_0^1 \int_{\mathcal{R}_E} \theta_k \theta_l \right) \mathbf{x}_{i,l}, \tag{38}$$

which is iterated together with the weak formulation for the solution (35).

Finally, in order to save further computation time, the space-time predictor solution $\mathbf{q}_i(\mathbf{x}, t)$ is integrated locally in time via Gauss-Legendre quadrature formula of appropriate order of accuracy such as:

$$\hat{\mathbf{q}}_i(\mathbf{x}) = \int_{t^n}^{t^{n+1}} \mathbf{q}_i(\mathbf{x}, t) dt; \tag{39}$$

which defines the predictor solution $\hat{\mathbf{q}}_i(\mathbf{x})$. This can then be used in order to obtain a fully-discrete one-step scheme based on the numerical fluxes between particles $\mathcal{P}_i$ and $\mathcal{P}_j$ as follows:

$$V_i^{n+1} \mathbf{q}_i^{n+1} = V_i^n \mathbf{q}_i^n - \sum_{j=1}^{N} V_i V_j 2\mathbf{G}_{ij} \left(\hat{\mathbf{q}}_{ij}^-(\mathbf{x}), \hat{\mathbf{q}}_{ij}^+(\mathbf{x}) \right) \cdot \nabla W_{ij} \, dt, \tag{40}$$

$$V_i^{n+1} = V_i^n + \sum_{j=1}^{N} \left(\hat{\mathbf{v}}_{ij} - \hat{\mathbf{v}}_i \right) \cdot \nabla W_{ij} \, dt, \tag{41}$$

$$\mathbf{r}_i^{n+1} = \mathbf{r}_i^n + \hat{\mathbf{v}}_i \, dt, \tag{42}$$

where all temporal integrals are properly taken into account in $\hat{\mathbf{q}}_{ij}$, $\hat{\mathbf{v}}_{ij}$ and $\hat{\mathbf{v}}_i$ through Equation (39). Since the space predictor solution integrated locally in time is known for all $\mathbf{x}$, the above scheme is a fully-discrete one-step scheme that does not require intermediate Runge-Kutta stages.

3. Numerical test cases

In this section we verify the effectiveness of the ADER-WENO-SPH method proposed in this paper. In particular, we compare the new ADER-WENO-SPH scheme with the RK-WENO-SPH method based on Runge-Kutta time integration, the first order Vila and Ben Moussa SPH scheme (hereafter refered as V&BM) and the standard SPH method of Gingold and Monaghan. In all test cases, we apply the Rusanov approximate Riemann solver. For the time integration algorithm we employ a third order TVD Runge-Kutta scheme for RK-WENO-SPH, V&BM as well as for the standard SPH. In all test cases the Courant-Friedrichs-Lewy condition has been used setting the CFL parameter equal to 0.4.

3.1. Circular blast wave problem

The aim of this test case is to compare the new ADER-WENO-SPH with the RK-WENO-SPH in order to define its accuracy and effectiveness in saving computational time, which establishes the main objects of extending the ADER reconstruction into the SPH framework.

For the Euler equations of compressible gas dynamics, the vector of conservative variables $\mathbf{q}$ and the flux tensor $\mathbf{F} = (\mathbf{f}, \mathbf{g})$ in the System (1) reads:

$$\mathbf{q} = \begin{pmatrix} \rho \\ \rho u \\ \rho v \\ E \end{pmatrix}, \qquad \mathbf{f} = \begin{pmatrix} \rho u \\ \rho u^2 + p \\ \rho uv \\ u(E+p) \end{pmatrix}, \qquad \mathbf{g} = \begin{pmatrix} \rho v \\ \rho uv \\ \rho v^2 + p \\ v(E+p) \end{pmatrix}, \tag{43}$$

where ρ is the fluid density; $\mathbf{v} = (u, v)$ is the velocity vector; p is the pressure; and e is the specific internal energy per unit mass, which, for ideal gases, is computed according the following constitutive equation:

$$e = \frac{p}{(\gamma - 1)\rho}, \tag{44}$$

where γ is a constant representing the ratio of specific heat capacities of the fluid (Cheng and Shu, 2007; Toro, 1997). Similarly, the pressure p can be written as follows:

$$p = (\gamma - 1)\left(E - \frac{1}{2}\rho\left(u^2 + v^2\right)\right), \tag{45}$$

where, E is the total energy per unit volume defined as

$$E = \rho e + \frac{1}{2}\rho\left(u^2 + v^2\right). \tag{46}$$

For the two dimensional blast wave problem, the computational domain is chosen as a circle with radius R=1.5 and center $(0, 0)$ discretized with 70933 particles located on a regular and radially symmetric grid and by choosing the following parameters as $\sigma = 2$, $\sigma_{mls} = 4$, $M = 2$ and $\gamma = 1.4$. In addition, the initial conditions have been set up according to the Sod (1978)'s test problem which reads as:

$$(\rho, u, v, p)(\mathbf{r}, 0) = \begin{cases} (\rho_{in}, 0, 0, p_{in}), & \text{if } \|\mathbf{r}\| \leq 0.5, \\ (\rho_{out}, 0, 0, p_{out}), & \text{otherwise,} \end{cases} \tag{47}$$

where the subscripts *in* and *out* denote the inner and the outer states, similar to the left and right states of a classic Riemann problem in 1D. The numerical results are compared with a radial reference solution of the one-dimensional Euler equations with a geometrical source term, see section 17.5 of Toro (1997) for details. Furthermore, two configurations have been chosen in order to properly evaluate the ADER-WENO-SPH scheme: the *blast wave problem EP1*, whose initial states are reported in Table (1); and the *blast wave problem EP2*, whose initial states are reported in Table (2).

Blast wave problem EP1: From Figures (3a,3b), it can be noticed that ADER-WENO-SPH is able to reproduce a numerical solution very similar to RK-WENO-SPH by modeling correctly both the discontinuities and the rarefaction waves. On the contrary, the standard SPH method (Figure 3d) exhibits a lot of spurious oscillations while the V&BM scheme (3c) presents an excessive amount of numerical dissipation. For the sake of completeness, Figure (4) shows the two dimensional solutions for density and pressure fields. In both cases, there are no oscillations and the ADER-WENO-SPH scheme preserves the radial symmetry properly.

Blast wave problem EP2: The wave problem EP2 is solved, with initial data given in Table (2) by using ADER-WENO-SPH and V&BM. As it can be noticed in Figure (5),the ADER-WENO-SPH scheme outperforms the standard V&BM formulation in simulating both density and pressure. This further underline that the ADER-WENO-SPH is able improve simulation accuracy also in test case characterized by strong shock waves.

3.1.1. Computational performance

In order to assess the computational performance, both ADER-WENO-SPH and RK-WENO-SPH have been parallelized by using the MPI paradigm, which is a widely used standard on modern massively parallel distributed-memory supercomputers. A performance benchmark problem has been computed considering the EP1 problem described in Section (3.1), but using periodic boundary conditions and a square computational domain $\Omega = [1.5; 1.5] \times [1.5; 1.5]$, where 22500 particles are distributed on a regular Cartesian lattice. This setup allows a proper distribution of the particles onto different processors so that each CPU core has the same amount of particles at the beginning of each simulation, avoiding load unbalance between processors.

Figure (6) shows the CPU times of both ADER-WENO-SPH and RK-WENO-SPH, using an increasing number of processors (2, 4, 8, 16, and 32). As it can be noticed, the ADER-WENO-SPH approach reduces the computational time by about 50% compared to RK-WENO-SPH in all cases. Moreover, the scalability of the two schemes are compared with the optimal theoretical performance (supposing 100 % MPI efficiency), showing that both SPH approaches based on MLS-WENO reconstruction in space have a very good parallel scalability.

3.2. Weakly compressible 2D vortex

The aim of this section is to further compare ADER-WENO-SPH with RK-WENO-SPH, V&BM and standard SPH by performing a convergence analysis where several number of particles are being used in order to discretize the computational domain as well as by considering different order of reconstructing polynomials.

We consider a weakly compressible 2D vortex where the Euler equation system (43) is written in cylindrical coordinates. This is characteristic by null radial velocity v_r and circumferential velocity component v_θ which depends exclusively on to the radial distance to the origin r with $r = \sqrt{x^2 + y^2}$, $v_r = ucos(\theta) + vsin(\theta)$, $v_\theta = -usin(\theta) + vcos(\theta)$ and $tan(\theta) = y/x$. This results in a steady state solution with radial symmetry which can be written as follows:

$$\begin{cases} \rho = \rho_0 + (\rho_M - \rho_0)\left(1 - \frac{2r}{r_0} e^{-\frac{2r}{r_0}} - e^{-\frac{2r}{r_0}}\right), \\ u_\theta = \frac{2r}{r_0} c_0 \sqrt{\frac{\rho_M - \rho_0}{\rho(r)}} e^{-\frac{2r}{r_0}}, \end{cases} \tag{48}$$

where ρ_M is the asymptotic density value; c_0 is the speed of sound; and ρ_0 is the reference density. Additionally, in this test case we use the so called Tait's equation in order computes the relative pressure field assuming the atmospheric reference pressure equal to zero. This reads as:

$$p = c_0^2(\rho - \rho_0), \tag{49}$$

which reduces System (1) to:

$$\mathbf{q} = \begin{pmatrix} \rho \\ \rho u \\ \rho v \end{pmatrix}, \qquad \mathbf{f} = \begin{pmatrix} \rho u \\ \rho u^2 + p \\ \rho uv \end{pmatrix}, \qquad \mathbf{g} = \begin{pmatrix} \rho v \\ \rho uv \\ \rho v^2 + p \end{pmatrix}. \tag{50}$$

The following parameterization has been adopted: $\rho_0 = 1.0 kg/m^2$; $\rho_M = 1.01 kg/m^2$; $r_0 = 0.1m$; and $c_0 = 1.0m/s$ while the computational domain is a circle with radius equal to $1.6m$. Regarding the numerical simulation, we have adopted $\sigma = 2$, $\sigma_{mls} = 4$ and the final time step has been fixed at $t = 2.0$.

The numerical convergence and accuracy results obtained by using different MLS and ADER polynomial reconstruction order are shown in Table (3) for density and in Table (4) for velocity, where Δx denotes the initial distance between particles used to discretize the computational domain. The errors and the convergence rates are shown in L_1, L_2 and L_∞ norms. In particular, L_1, L_2 are computed according to:

$$L_q = \left(\frac{\sum_{j=1}^{N_p} |q_n - q_e|^q}{N_p} \right)^{1/q}; \tag{51}$$

where q_n is the numerical solution while q_e is the given exact solution. The L_∞ norm is instead computed by taking the maximum error among all particles.

Figure (7) shows that: both standard SPH and V&BM exhibit very poor convergence rate for density as well as for velocity; standard SPH, as expected, shows negative convergence rates due to the disordered distribution of the particles; V&BM presents convergence rates close to zero in most of the cases; RK-WENO-SPH and ADER-WENO-SPH increase accuracy and convergence rates compared to standard SPH and V&BM schemes; RK-WENO-SPH and ADER-WENO-SPH present same behavior in terms of accuracy and convergence rate when second order reconstruction polynomials are used; and RK-WENO-SPH is slightly more accurate respect to ADER-WENO-SPH when third order reconstruction polynomials are adopted. These results are supported by Table (3) and by Table (4).

3.3. Magnetohydrodynamics test cases

The new ADER-WENO-SPH scheme presented in this paper has also been tested on the classical equations of ideal magnetohydrodynamics (MHD), which represents a more complex and interesting hyperbolic system, where, differently from the classical Euler equations, the numerical method must also satisfy the local divergence-free condition for the magnetic field $\nabla \cdot \mathbf{B} = 0$. Specifically, from a numerical point of view, the so called hyperbolic *divergence-cleaning* procedure is adopted here, which is based on the the generalized Lagrangian multiplier (GLM)

divergence cleaning method developed by Dedner et al. (2002). As a consequence, according to Dedner et al. (2002)'s scheme, an auxiliary variable φ and an additional scalar PDE are introduced in the original MHD system in order to propagate divergence errors in the magnetic field away. The resulting augmented MHD system written in conservative form reads as follows:

$$\mathbf{u} = \begin{pmatrix} \rho \\ \rho u v_i \\ E \\ B_j \\ \varphi \end{pmatrix}, \quad \mathbf{F}_i = \begin{pmatrix} \rho v_i \\ \rho v_i v_j \left(p + \mathbf{B}^2/8\pi\right)\delta_{ij} - B_i B_j/8\pi \\ \left(E + p + \mathbf{B}^2/8\pi\right) v_i - (\mathbf{v}\cdot\mathbf{B})\, B_i/4\pi \\ \epsilon_{ijk} E_k + \varphi\, \delta_{ij} \\ c_h^2 B_i \end{pmatrix}, \quad x, y, z = i, j, k, \tag{52}$$

where $\mathbf{B} = (B_x, B_y, B_z)$ is the magnetic field vector, $\mathbf{E} = -\mathbf{v}\times\mathbf{B}$ is the electric field vector, δ_{ij} is the Kronecker delta and ϵ_{ijk} is the Levi-Civita symbol. We point out that in Equation (52) the term c_h represents the so called divergence cleaning velocity which allows to transport possible divergence errors and thus spurious numerical magnetic monopoles out of the computational domain. Accordingly to Dedner et al. (2002)'s MHD formulation framework, Equation of state reads as:

$$p = \mathbf{E}(\gamma - 1) - \frac{\mathbf{v}^2}{2} - \frac{\mathbf{B}^2}{8\pi}. \tag{53}$$

In the following, we consider two well-known and nontrivial problems of classical ideal MHD: the MHD rotor and the Orszag-Tang vortex problems. The divergence cleaning velocity is set equal to $c_h = 4$ while the adiabatic index is $\gamma = 1.4$.

3.3.1. MHD rotor problem

The first test is the MHD rotor problem. This was described for the first time in Balsara and Spicer (1999). It consists in a high density fluid is rotating rapidly with angular velocity ω so that $\mathbf{v} = \boldsymbol{\omega}\times\mathbf{x}$ with $\boldsymbol{\omega} = (0, 0, \omega)$. This is inserted in a low density fluid in a two dimensional domain Ω. In the standard rotor problem test case the initial conditions are the following:

$$\rho = \begin{cases} 10, & \text{if } \|\mathbf{r}\| \le 0.1, \\ 1, & \text{otherwise,} \end{cases} \quad \omega = \begin{cases} 10, & \text{if } \|\mathbf{r}\| \le 0.1, \\ 0, & \text{otherwise,} \end{cases} \quad \mathbf{B} = \begin{pmatrix} 2.5 \\ 0 \\ 0 \end{pmatrix}, \quad p = 1. \tag{54}$$

The computational domain is discretized with 544357 equidistant particles placed with radial symmetry in a circle with radius $R = 0.6$.

Figure (8) shows the solution for density and pressure computed with the ADER-WENO-SPH and with the V&BM schemes at the time $t = 0.25s$. As it can be noticed, for the ADER-WENO-SPH case the results are in agreement with (Balsara and Spicer, 1999), (Dumbser et al., 2013) and (Zanotti et al., 2015), where high order mesh based schemes for ideal MHD have been applied.

On one hand, both ADER-WENO-SPH and V&BM do not present spurious oscillations. On the other, it is evident that the V&BM is not able to properly simulate the torsional Alfvén waves due to the higher numerical diffusion. The different behavior of ADER-WENO-SPH respect to V&BM is further underlined by the zoomed regions.

3.3.2. The Orszag-Tang vortex

The last test case is the well-known Orszag-Tang vortex problem (Orszag and Tang, 1979) studied for example in (Tricco et al., 2016) in the SPH framework or in (Dumbser and Zanotti, 2009) by using high order $P_N P_M$ schemes on unstructured meshes. Following (Zanotti et al., 2015), the computation domain is $\Omega = [0, 2\pi]^2$ with periodic boundary conditions everywhere. The initial conditions are given by:

$$\left(\rho, u, v, p, B_x, B_y\right) = (1 - \sin(y), \sin(x), 1, -B_0 \sin(y), B_0 \sin(2x)), \tag{55}$$

with $w = B_z = 0$ and $\gamma = 4/3$. The problem is solved up to $t = 2.5$ by using a third order reconstruction, where 201901 particles are initially distributed equidistantly in the computational domain Ω. Figure (9) shows the results computed with ADER-WENO-SPH and V&BM at different times. It can be noticed that, in contrast to first order V&BM

method, in the ADER-WENO-SPH scheme the smooth sinusoidal initial condition evolves in time to form complex shock dominated structures, in agreement with the reference solutions available in the literature (e.g. Dumbser et al., 2013; Zanotti et al., 2015). In addition, the zoomed regions in Figure (9) illustrate the different distributions of particles in the computational field as outcome of ADER-WENO-SPH or V&BM. Despite V&BM generates more regular particle distributions, the differences with particle distributions between V&BM and ADER-WENO-SPH is due to the higher numerical diffusion of V&BM formulation which particularly affects the advection component of equations and therefore the position of the particle. Figure (10) further underlines the differences between ADER-WENO-SPH and V&BM schemes. Specifically, this figure illustrates the density field along the section of the computation field with $x = \pi$. It is evident that V&BM scheme smooths the numerical solution form initial time steps. This results in an incapacity of the V&BM in capturing shock waves as well their interactions.

4. Conclusion

In this paper we have presented a novel family of ADER-WENO-SPH scheme that replaces the Runge-Kutta time stepping with high order reconstruction polynomials in space and time. In particular, the main idea has been to employ moving least-squares WENO reconstruction to obtain higher order space-time polynomials. This has been accomplished by means of the ADER approach, introduced in Toro and Titarev (2006); Dumbser et al. (2008b,a) and for first time here extended to meshless Lagrangian particle methods.

We have tested the ADER-WENO-SPH scheme by means of numerical test cases. The obtained numerical results indicate that: the novel ADER-WENO-SPH method outperforms existing SPH schemes in terms of accuracy and robustness; the new ADER-WENO-SPH method has performances in term of accuracy comparable to the RK-WENO-SPH; and the new ADER-WENO-SPH method is computationally more efficient than the RK-WENO-SPH.

Future work will concern the extension of the ADER-WENO-SPH method to the unified first order hyperbolic model of continuum mechanics forwarded by Godunov & Romenski and Peshkov & Romenski (GPR model) in Godunov (1961); Godunov and Romenski (1972, 2003); Romenski (1998); Peshkov and Romenski (2016); Dumbser et al. (2016) and in the appropriate treatment of boundary conditions in the ADER-WENO-SPH framework, which could be based on the so called fixed particles approach (Marrone et al., 2011; Crespo et al., 2015; Fourtakas et al., 2019); on a semi-analytical scheme (e.g. Kulasegaram et al., 2004); or following the methodology for ALE-SPH schemes presented in (Marongiu et al., 2010).

Acknowledgements

M.R. and D.A. acknowledge support from the project "Applied Thermo-Fluid Dynamics Laboratories. Applied Research Infrastructures for Companies and Industry in South Tyrol" (FESR1029), financed by the European Regional Development Fund (ERDF) Investment for Growth and Jobs Programme 2014-2020 and the Autonomous Province of Bolzano.

M.D. acknowledges funding from the Italian Ministry of Education, University and Research (MIUR) in the frame of the Departments of Excellence Initiative 2018–2022 attributed to DICAM of the University of Trento (grant L. 232/2016) and in the frame of the PRIN 2017 project *Innovative numerical methods for evolutionary partial differential equations and applications*. Furthermore, M.D. has also received funding from the University of Trento via the Strategic Initiative *Modeling and Simulation*.

5. Figures

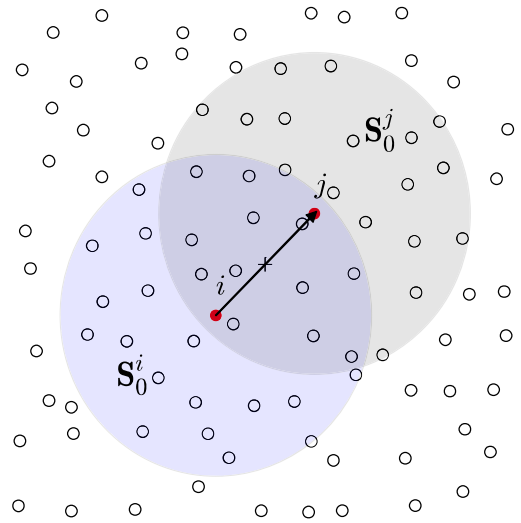

(a) Central stencils for particle *i-th* and *j-th*.

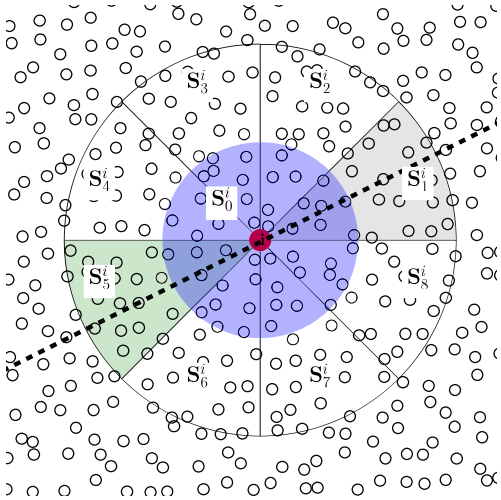

(b) Central stencil and lateral stencils for particle for the *i-th*.

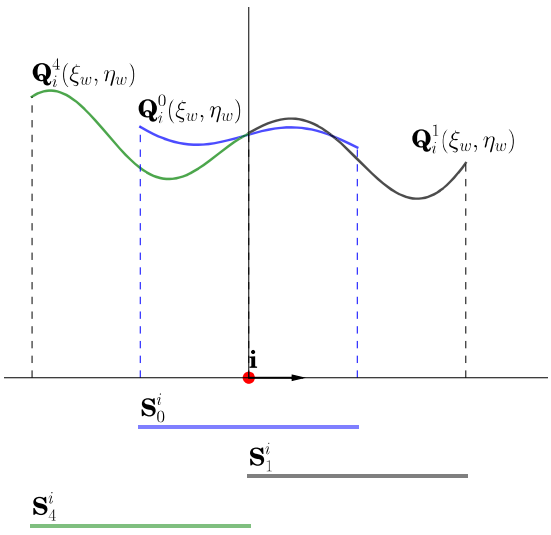

(c) Polynomial reconstructions for the central stencil S_0^i and stencils S_4^i, S_1^i

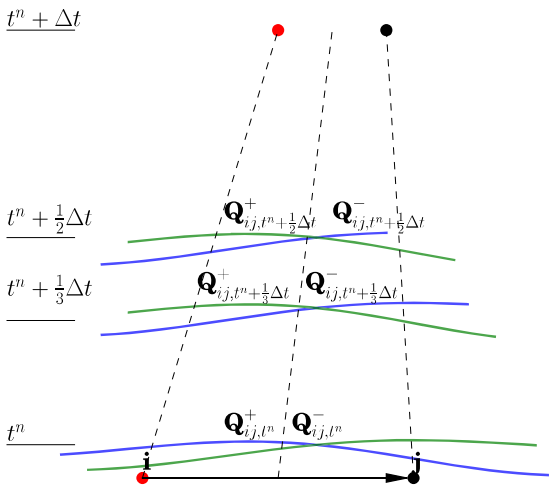

(d) Third order Runge-Kutta time integration of numerical fluxes between particles *i* and *j*.

Figure 1: Illustrative example of the MW-SPH scheme.

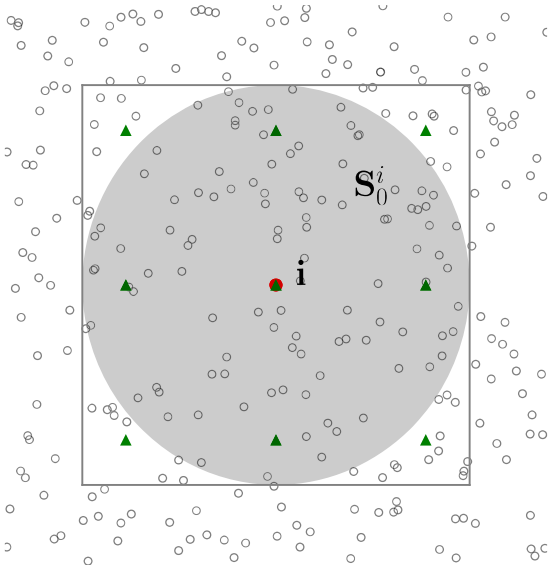

(a) Central stencils for particle *i-th* and Gauss-Lagrange points.

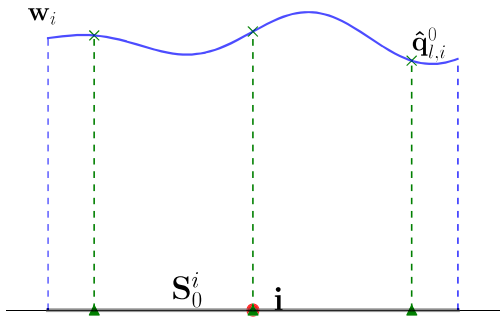

(b) WENO reconstruction polynomial $\mathbf{w}_i$ and polynomial value on Gauss-Lagrange points.

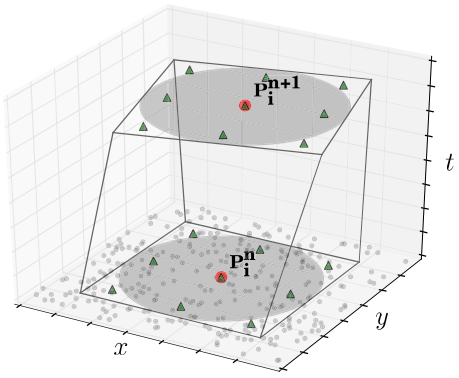

(c) Physical space-time element.

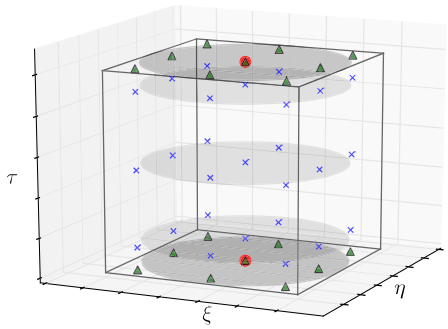

(d) Space-time reference element

Figure 2: Iso-parametric mapping of the space-time reference element to the physical space-time element using the local space-time Galerkin predictor for the particle i in the central stencil $\mathbf{S}_0$.

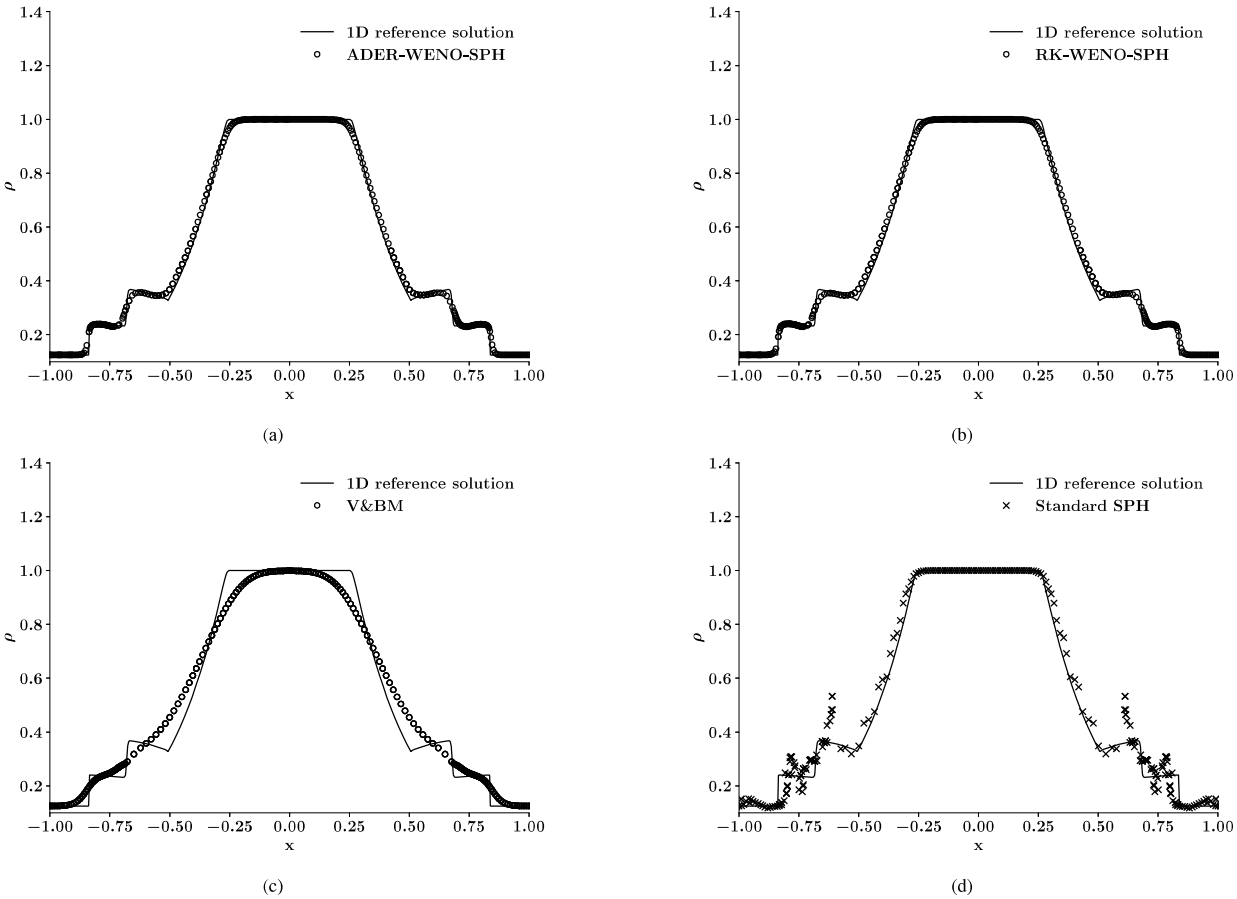

Figure 3: Two dimensional numerical results of the blast wave problem EP1 with ADER-WENO-SPH, RK-WENO-SPH, V&BM SPH and standard SPH at time $t = 0.2$, where $\sigma = 2$, $\sigma_{mls} = 4$, $M = 2$, $\gamma = 1.4$ and $CFL = 0.5$. Cut at $y = 0$ compared with 1D reference solution (continuous line).

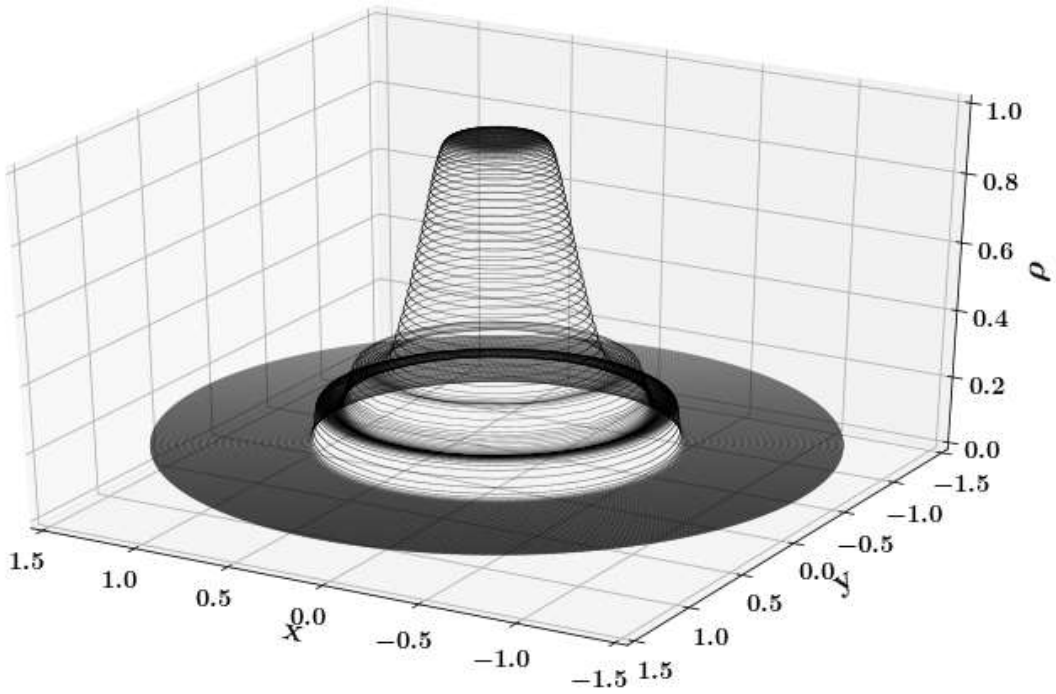

(a)

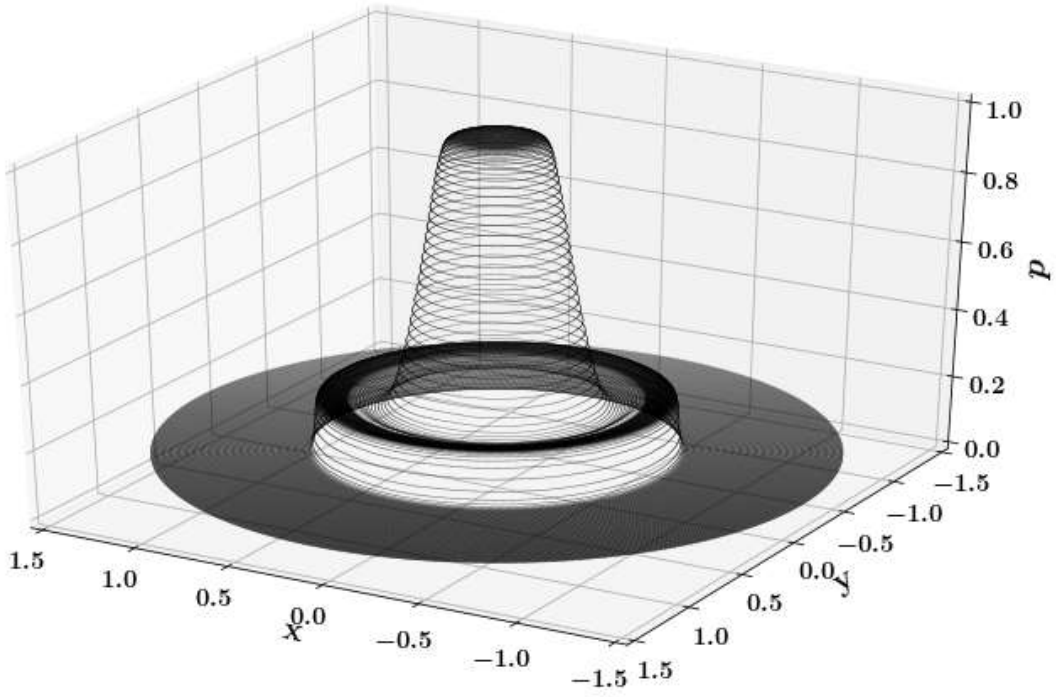

(b)

Figure 4: Numerical results for the two-dimensional blast wave problem EP1 obtained with the new ADER-WENO-SPH at time $t = 0.2$ for density ρ and pressure p, where $\sigma = 2$, $\sigma_{mls} = 4$, $M = 2$, $\gamma = 1.4$, $CFL = 0.5$.

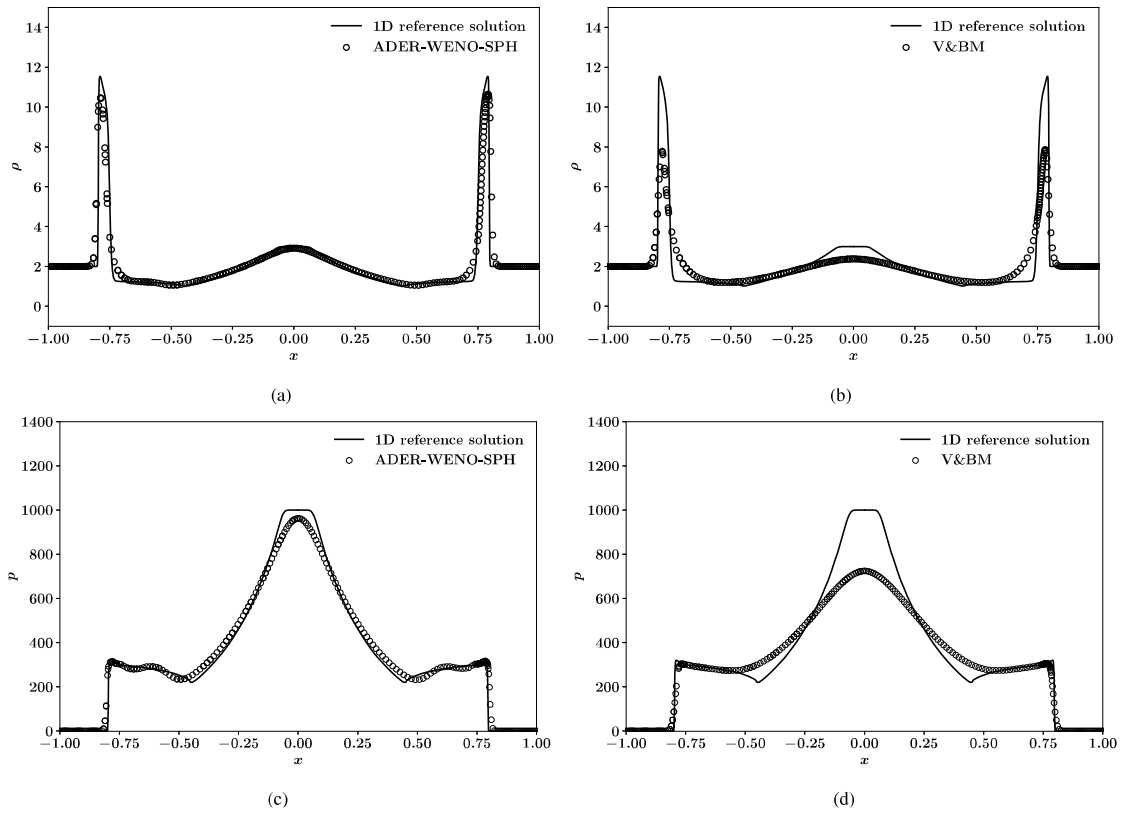

Figure 5: Two dimensional numerical results of the blast wave problem EP2 with ADER-WENO-SPH and V&BM at time $t = 0.02$, where $\sigma = 2$, $\sigma_{mls} = 4$, $M = 2$, $\gamma = 1.4$. Cut at $y = 0$ compared with 1D reference solution (continuous line).

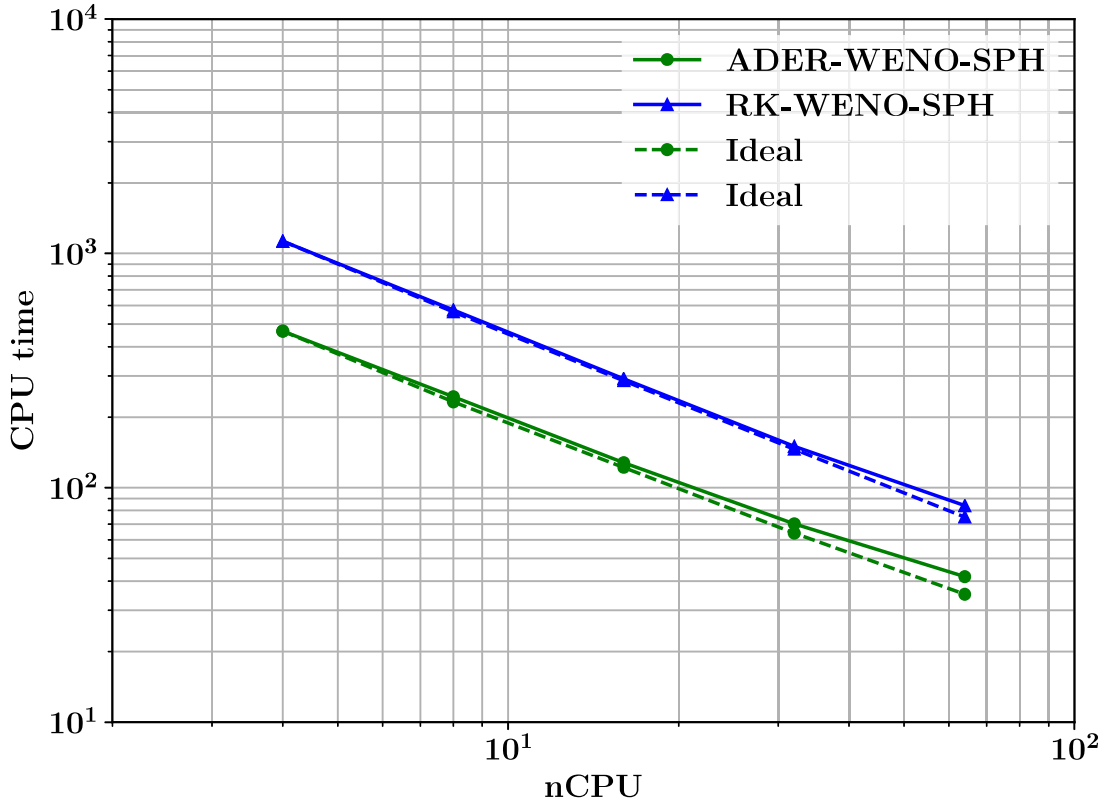

Figure 6: Speed-up graph, comparing the measured (solid line) and the ideal (dashed line) wall-clock times from 2 to 32 CPU cores for ADER-WENO-SPH and RK-WENO-SPH.

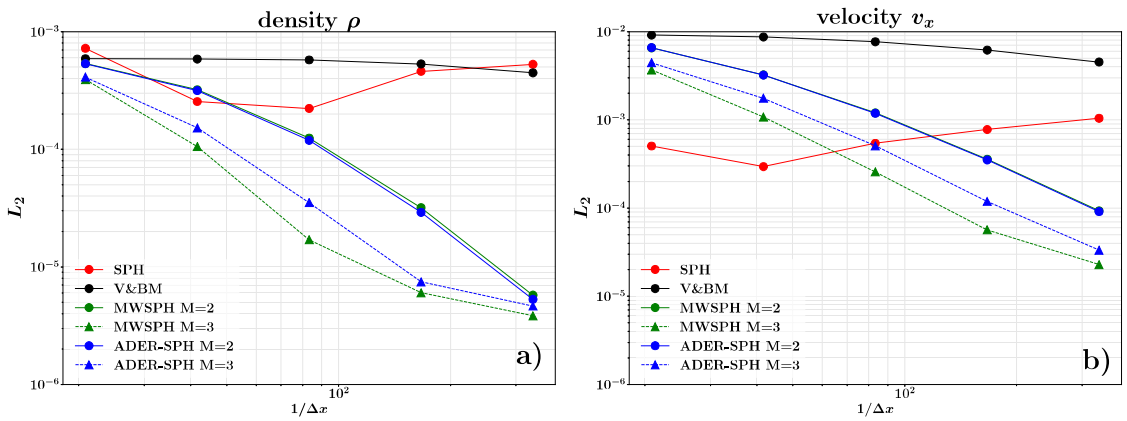

Figure 7: L_2 error with respect to initial particle distance for the weakly compressible 2D vortex test case computed with standard SPH, V&BM, RK-WENO-SPH and ADER-WENO-SPH: a) for density ρ and b) for velocity v_x.

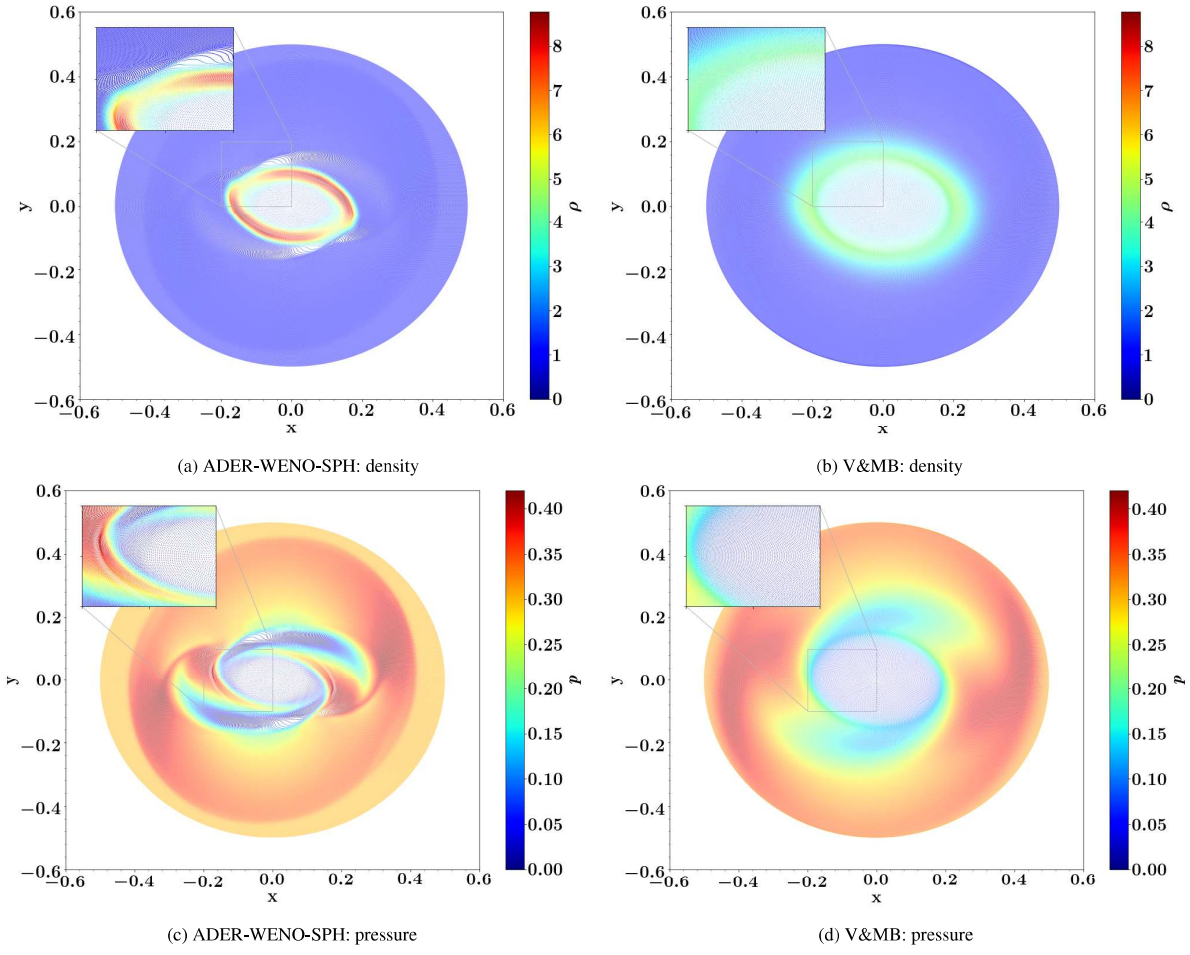

(a) ADER-WENO-SPH: density

(b) V&MB: density

(c) ADER-WENO-SPH: pressure

(d) V&MB: pressure

Figure 8: Density field, pressure field computed with ADER-WENO-SPH (on the left) and with V&MB (on the right) at time $t = 0.25$, 544357 particles, $\gamma = 1.4$, $M = 2$, $\sigma = 2$, $\sigma_{mls} = 4$, $CFL = 0.5$, $c_h = 4$.

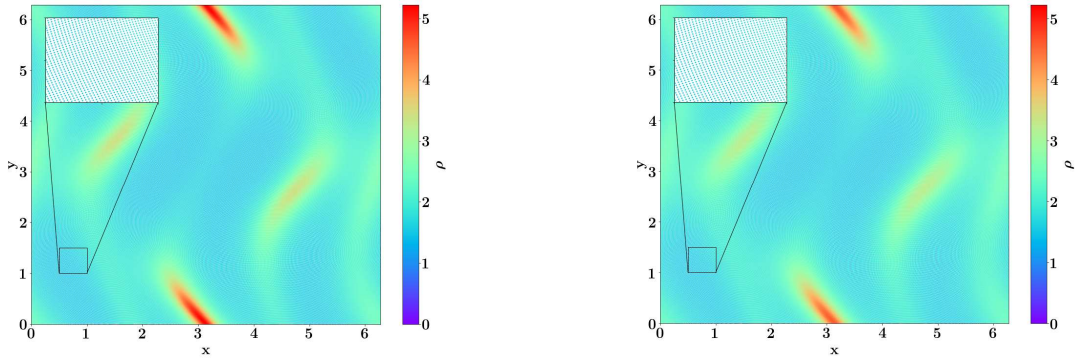

(a) ADER-WENO-SPH, time $t = 0.5$.

(b) V&BM, time $t = 0.5$.

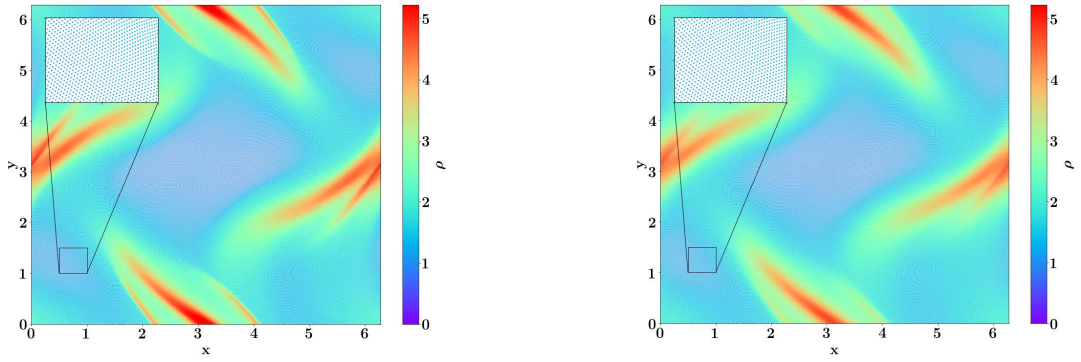

(c) ADER-WENO-SPH, time $t = 1$.

(d) V&BM, time $t = 1$

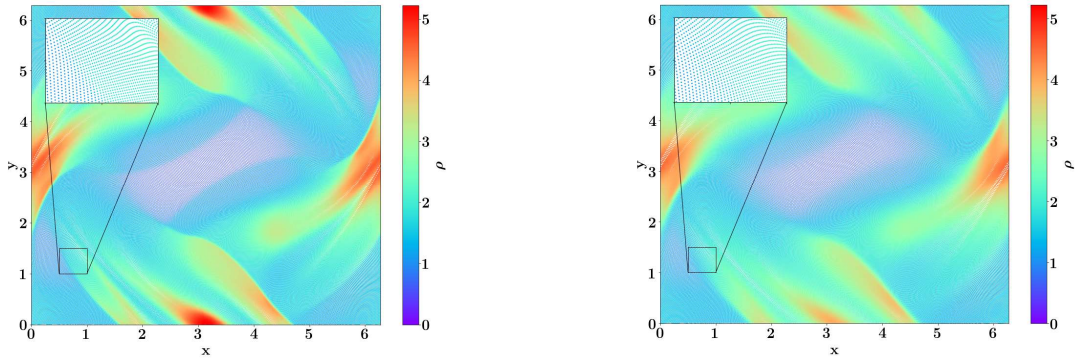

(e) ADER-WENO-SPH, time $t = 1.5$.

(f) V&BM, time $t = 1.5$.

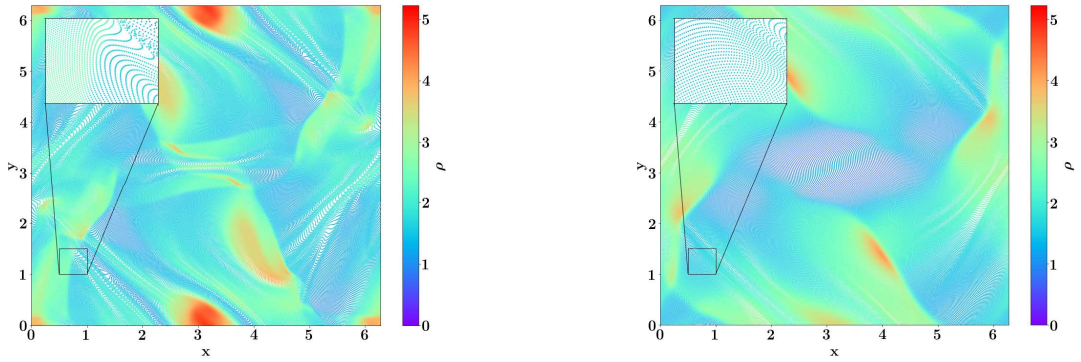

(g) ADER-WENO-SPH, time $t = 2$

(h) V&BM, time $t = 2$

Figure 9: Density field for the Orszag-Tang vortex problem solved with ADER-WENO-SPH (left) and the V&BM (right) using 201901 particles at time $t = 0.5$, $t = 1$, $t = 1.5$, $t = 2$, where $\gamma = 1.4$, $M = 2$, $\sigma = 2$, $\sigma_{mls} = 4$, $CFL = 0.5$ and $c_h = 4$.

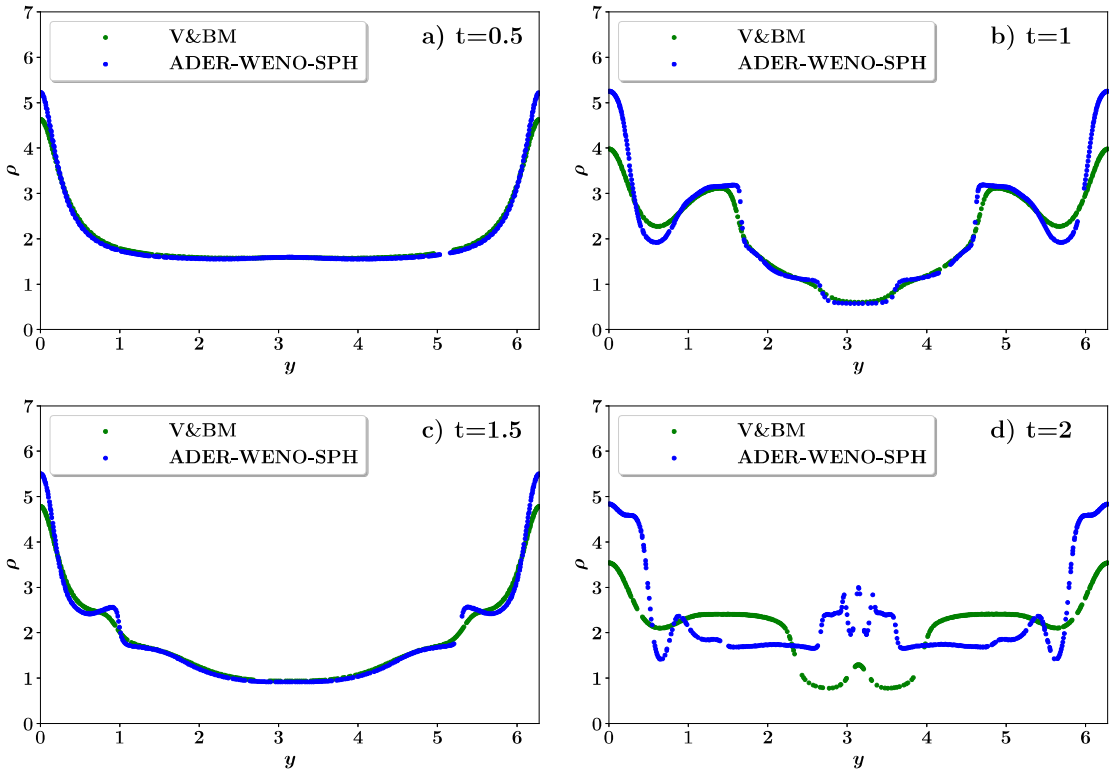

Figure 10: Comparison of the density field for the Orszag-Tang vortex problem solved with ADER-WENO-SPH (left) and the V&BM (right) at different times. The density field is shown along the section with x=π

	ρ	u	v	p
$\mathbf{q}_{in}$	1.0	0.0	0.0	1.0
$\mathbf{q}_{out}$	0.125	0.0	0.0	0.1

Table 1: Initial states $\mathbf{q}_{in}$ (inner) and $\mathbf{q}_{out}$ (outer) for two-dimensional blast wave problem EP1.

	ρ	u	v	p
$\mathbf{q}_{in}$	3.0	0.0	0.0	1000.0
$\mathbf{q}_{out}$	2.0	0.0	0.0	0.1

Table 2: Initial states $\mathbf{q}_{in}$ (inner) and $\mathbf{q}_{out}$ (outer) for two-dimensional blast wave problem EP2.

dx	ϵ_{L_1}	ϵ_{L_2}	ϵ_{L_∞}	$O(L_1)$	$O(L_2)$	$O(L_\infty)$
standard SPH						
4.80E-02	4.11E-04	7.22E-04	2.57E+02	-	-	-
2.40E-02	1.39E-04	2.55E-04	5.12E-03	1.57	1.50	2.33
1.20E-02	1.31E-04	2.23E-04	1.31E-02	0.09	0.19	-1.35
6.00E-03	2.90E-04	4.60E-04	2.73E-02	-1.15	-1.15	-1.06
3.00E-03	3.56E-04	5.28E-04	3.89E-02	-0.30	-0.20	-0.51
V&BM						
4.80E-02	9.88E-05	5.89E-01	3.25E+00	-	-	-
2.40E-02	9.66E-05	5.85E-01	1.05E-01	0.03	0.01	1.63
1.20E-02	9.03E-05	5.75E-02	1.70E-01	0.10	0.03	-0.69
6.00E-03	7.79E-05	5.32E-02	1.63E-02	0.21	0.11	0.06
3.00E-03	6.29E-05	4.47E-03	2.94E-03	0.31	0.25	-0.86
RK-WENO-SPH (M=2)						
4.80E-02	1.09E-04	5.35E-04	3.04E+02	-	-	-
2.40E-02	3.96E-05	3.21E-04	7.59E-03	1.46	0.74	2.00
1.20E-02	1.20E-05	1.25E-04	3.94E-03	1.72	1.37	0.95
6.00E-03	2.51E-06	3.19E-05	1.47E-03	2.25	1.97	1.42
3.00E-03	5.77E-07	5.75E-06	5.31E-04	2.12	2.47	1.47
RK-WENO-SPH (M=3)						
4.80E-02	7.35E-05	3.92E-04	2.43E+02	-	-	-
2.40E-02	9.91E-06	1.05E-04	3.49E-03	2.89	1.89	2.80
1.20E-02	1.73E-06	1.70E-05	1.01E-03	2.52	2.63	1.79
6.00E-03	8.09E-07	6.03E-06	1.83E-04	1.10	1.50	2.46
3.00E-03	5.09E-07	3.84E-06	3.22E-04	0.67	0.65	-0.81
ADER-WENO-SPH (M=2)						
4.80E-02	1.03E-04	5.34E-04	3.04E-02	-	-	-
2.40E-02	3.84E-05	3.15E-04	7.54E-03	1.43	0.76	2.01
1.20E-02	1.13E-05	1.19E-04	3.85E-03	1.76	1.40	0.97
6.00E-03	2.38E-06	2.91E-05	1.42E-03	2.24	2.03	1.44
3.00E-03	6.20E-07	5.30E-06	5.37E-04	1.94	2.46	1.40
ADER-WENO-SPH (M=3)						
4.80E-02	6.49E-05	4.10E-04	2.53E-02	-	-	-
2.40E-02	1.85E-05	1.52E-04	4.60E-03	1.81	1.43	2.46
1.20E-02	4.28E-06	3.52E-05	1.81E-03	2.11	2.11	1.35
6.00E-03	1.16E-06	7.46E-06	4.12E-04	1.88	2.24	2.13
3.00E-03	6.76E-07	4.64E-06	3.73E-04	0.78	0.68	0.14

Table 3: Numerical convergence results for standard SPH, V&BM, RK-WENO-SPH and ADER-WENO-SPH for density ρ. In the first row the particles distance dx. The second, third and fourth columns contain the error measured in L_1, L_2 and L_∞ norms, followed by three columns giving the measured order of accuracy between the respective particles and the previous particles distributions.

dx	ϵ_{L_1}	ϵ_{L_2}	ϵ_{L_∞}	$O(L_1)$	$O(L_2)$	$O(L_\infty)$
standard SPH						
4.80E-02	1.98E-04	5.05E-04	3.56E-02	-	-	-
2.40E-02	1.97E-04	2.96E-04	5.91E-03	0.00	0.77	2.59
1.20E-02	3.36E-04	5.43E-04	2.91E-02	-0.77	-0.88	-2.30
6.00E-03	4.85E-04	7.78E-04	5.07E-02	-0.53	-0.52	-0.80
3.00E-03	6.80E-04	1.04E-03	8.77E-02	-0.49	-0.42	-0.79
V&BM						
4.80E-02	2.84E-03	9.15E-03	2.77E-01	-	-	-
2.40E-02	2.74E-03	8.71E-03	1.25E-01	0.05	0.07	1.15
1.20E-02	2.29E-03	7.69E-03	2.38E-01	0.26	0.18	-0.93
6.00E-03	1.66E-03	6.20E-03	1.91E-01	0.47	0.31	0.32
3.00E-03	1.07E-03	4.53E-03	1.96E-01	0.63	0.45	-0.04
RK-WENO-SPH (M=2)						
4.80E-02	1.68E-03	6.56E-03	2.35E-01	-	-	-
2.40E-02	6.83E-04	3.24E-03	6.56E-02	1.30	1.02	1.84
1.20E-02	1.79E-04	1.20E-03	3.71E-02	1.93	1.43	0.82
6.00E-03	4.42E-05	3.58E-04	1.22E-02	2.02	1.74	1.61
3.00E-03	1.58E-05	9.32E-05	9.46E-03	1.48	1.94	0.36
RK-WENO-SPH (M=3)						
4.80E-02	8.21E-04	3.68E-03	1.64E-01	-	-	-
2.40E-02	1.69E-04	1.08E-03	2.65E-02	2.28	1.77	2.63
1.20E-02	3.47E-05	2.58E-04	1.10E-02	2.28	2.06	1.27
6.00E-03	1.42E-05	5.66E-05	3.96E-03	1.29	2.19	1.47
3.00E-03	1.05E-05	2.29E-05	2.13E-03	0.43	1.31	0.89
ADER-WENO-SPH (M=2)						
4.80E-02	1.69E-03	6.59E-03	2.35E-01	-	-	-
2.40E-02	6.81E-04	3.23E-03	6.55E-02	1.31	1.03	1.84
1.20E-02	1.77E-04	1.19E-03	3.66E-02	1.94	1.44	0.84
6.00E-03	4.44E-05	3.52E-04	1.23E-02	2.00	1.75	1.58
3.00E-03	1.64E-05	9.13E-05	1.23E-02	1.44	1.95	0.00
ADER-WENO-SPH (M=3)						
4.80E-02	9.91E-04	4.45E-03	1.89E-01	-	-	
2.40E-02	3.05E-04	1.76E-03	4.09E-02	1.70	1.34	2.20
1.20E-02	6.87E-05	5.08E-04	1.71E-02	2.15	1.79	1.26
6.00E-03	2.07E-05	1.19E-04	6.30E-03	1.73	2.09	1.44
3.00E-03	1.20E-05	3.33E-05	4.22E-03	0.79	1.84	0.58

Table 4: Numerical convergence results for standard SPH, V&BM, RK-WENO-SPH and ADER-WENO-SPH for velocity v_x. In the first row the particles distance dx. The second, third and fourth columns contain the error measured in L_1, L_2 and L_∞ norms, followed by three columns giving the measured order of accuracy between the respective particles and the previous particles distributions.

References

Agossler Albert, A., 2001. Moving Least-Squares: A Numerical Differentiation Method for Irregularly Spaced Calculation Points. Technical Report. Sandia National Labs. doi:10.2172/782718.

Antuono, M., Colagrossi, A., Marrone, S., Molteni, D., 2010. Free-surface flows solved by means of sph schemes with numerical diffusive terms. Computer Physics Communications 181, 532 – 549. URL: http://www.sciencedirect.com/science/article/pii/S0010465509003506, doi:https://doi.org/10.1016/j.cpc.2009.11.002.

Avesani, D., Dumbser, M., Bellin, A., 2014. A new class of moving-least-squares weno–sph schemes. Journal of Computational Physics 270, 278 – 299. URL: http://www.sciencedirect.com/science/article/pii/S0021999114002289, doi:https://doi.org/10.1016/j.jcp.2014.03.041.

Avesani, D., Dumbser, M., Chiogna, G., Bellin, A., 2017. An alternative smooth particle hydrodynamics formulation to simulate chemotaxis in porous media. Journal of Mathematical Biology 74, 1037–1058. URL: https://doi.org/10.1007/s00285-016-1049-6, doi:10.1007/s00285-016-1049-6.

Avesani, D., Herrera, P., Chiogna, G., Bellin, A., Dumbser, M., 2015. Smooth particle hydrodynamics with nonlinear moving-least-squares weno reconstruction to model anisotropic dispersion in porous media. Advances in Water Resources 80, 43 – 59. URL: http://www.sciencedirect.com/science/article/pii/S0309170815000627, doi:https://doi.org/10.1016/j.advwatres.2015.03.007.

Balsara, D.S., Spicer, D.S., 1999. A staggered mesh algorithm using high order godunov fluxes to ensure solenoidal magnetic fields in magnetohydrodynamic simulations. Journal of Computational Physics 149, 270 – 292. URL: http://www.sciencedirect.com/science/article/pii/S0021999198961538, doi:https://doi.org/10.1006/jcph.1998.6153.

Bassi, F., Botti, L., Colombo, A., Pietro, D.D., Tesini, P., 2012. On the flexibility of agglomeration based physical space discontinuous galerkin discretizations. Journal of Computational Physics 231, 45 – 65. URL: http://www.sciencedirect.com/science/article/pii/S0021999111005055, doi:https://doi.org/10.1016/j.jcp.2011.08.018.

Ben Moussa, B., 2006. On the convergence of sph method for scalar conservation laws with boundary conditions. Method Appl Anal , 29–62.

Ben Moussa, B., Lanson, N., Vila, J., 1999. On the convergence of sph method for scalar conservation laws with boundary conditions. Int Ser Numer Math , 31–40.

Boscheri, W., Dumbser, M., 2013. Arbitrary–Lagrangian–Eulerian One–Step WENO Finite Volume Schemes on Unstructured Triangular Meshes. Communications in Computational Physics 14, 1174–1206.

Boscheri, W., Dumbser, M., 2014. A direct Arbitrary-Lagrangian-Eulerian ADER-WENO finite volume scheme on unstructured tetrahedral meshes for conservative and non-conservative hyperbolic systems in 3D. Journal of Computational Physics 275, 484 – 523.

Boscheri, W., Dumbser, M., 2017. Arbitrary–Lagrangian–Eulerian Discontinuous Galerkin schemes with a posteriori subcell finite volume limiting on moving unstructured meshes. Journal of Computational Physics 346, 449–479.

Boscheri, W., Dumbser, M., Balsara, D., 2014. High Order Lagrangian ADER-WENO Schemes on Unstructured Meshes – Application of Several Node Solvers to Hydrodynamics and Magnetohydrodynamics. International Journal for Numerical Methods in Fluids 76, 737–778.

Busto, S., Chiocchetti, S., Dumbser, M., Gaburro, E., Peshkov, I., 2020. High order ADER schemes for continuum mechanics. Frontiers in Physics 8, 32. DOI: 10.3389/fphy.2020.00032.

Chen, J.K., Beraun, J.E., Carney, T.C., 1999. A corrective smoothed particle method for boundary value problems in heat conduction. International Journal for Numerical Methods in Engineering 46, 231–252. doi:10.1002/(SICI)1097-0207(19990920)46:2¡231::AID-NME672¿3.0.CO;2-K.

Cheng, J., Shu, C.W., 2007. A high order {ENO} conservative lagrangian type scheme for the compressible euler equations. Journal of Computational Physics 227, 1567 – 1596. URL: http://www.sciencedirect.com/science/article/pii/S002199910700424X, doi:http://dx.doi.org/10.1016/j.jcp.2007.09.017.

Clain, S., Diot, S., Loubère, R., 2011. A high-order finite volume method for systems of conservation laws—multi-dimensional optimal order detection (MOOD). Journal of Computational Physics 230, 4028 – 4050.

Cravero, I., Puppo, G., Semplice, M., Visconti, G., 2018. CWENO: uniformly accurate reconstructions for balance laws. Math. Comp. 87, 1689–1719.

Crespo, A., Domínguez, J., Rogers, B., Gómez-Gesteira, M., Longshaw, S., Canelas, R., Vacondio, R., Barreiro, A., García-Feal, O., 2015. Dualsphysics: Open-source parallel cfd solver based on smoothed particle hydrodynamics (sph). Computer Physics Communications 187, 204–216. URL: https://www.sciencedirect.com/science/article/pii/S0010465514003397, doi:https://doi.org/10.1016/j.cpc.2014.10.004.

Dedner, A., Kemm, F., Kröner, D., Munz, C.D., Schnitzer, T., Wesenberg, M., 2002. Hyperbolic Divergence Cleaning for the MHD Equations. Journal of Computational Physics 175, 645–673. doi:10.1006/jcph.2001.6961.

Dilts, G.A., 1999. Moving-least-squares-particle hydrodynamics—i. consistency and stability. International Journal for Numerical Methods in Engineering 44, 1115–1155. URL: http://dx.doi.org/10.1002/(SICI)1097-0207(19990320)44:8<1115::AID-NME547>3.0.CO;2-L, doi:10.1002/(SICI)1097-0207(19990320)44:8¡1115::AID-NME547¿3.0.CO;2-L.

Diot, S., Clain, S., Loubère, R., 2012. Improved detection criteria for the multi-dimensional optimal order detection (MOOD) on unstructured meshes with very high-order polynomials. Computers and Fluids 64, 43 – 63.

Diot, S., Loubère, R., Clain, S., 2013. The MOOD method in the three-dimensional case: Very-high-order finite volume method for hyperbolic systems. International Journal of Numerical Methods in Fluids 73, 362–392.

Dumbser, M., Balsara, D.S., Toro, E.F., Munz, C.D., 2008a. A unified framework for the construction of one-step finite volume and discontinuous galerkin schemes on unstructured meshes. Journal of Computational Physics 227, 8209 – 8253. URL: http://www.sciencedirect.com/science/article/pii/S0021999108002829, doi:10.1016/j.jcp.2008.05.025.

Dumbser, M., Boscheri, W., Semplice, M., Russo, G., 2017. Central weighted ENO schemes for hyperbolic conservation laws on fixed and moving unstructured meshes. SIAM Journal on Scientific Computing 39, A2564–A2591.

Dumbser, M., Enaux, C., Toro, E.F., 2008b. Finite volume schemes of very high order of accuracy for stiff hyperbolic balance laws. Journal of Computational Physics 227, 3971 – 4001. URL: http://www.sciencedirect.com/science/article/pii/S0021999107005578, doi:10.1016/j.jcp.2007.12.005.

Dumbser, M., Käser, M., 2007. Arbitrary high order non-oscillatory finite volume schemes on unstructured meshes for linear hyperbolic systems.

Journal of Computational Physics 221, 693–723. URL: http://www.sciencedirect.com/science/article/pii/S0021999106003123, doi:10.1016/j.jcp.2006.06.043.

Dumbser, M., Käser, M., Titarev, V.A., Toro, E.F., 2007. Quadrature-free non-oscillatory finite volume schemes on unstructured meshes for nonlinear hyperbolic systems. Journal of Computational Physics 226, 204 – 243. URL: http://www.sciencedirect.com/science/article/pii/S0021999107001520, doi:10.1016/j.jcp.2007.04.004.

Dumbser, M., Peshkov, I., Romenski, E., Zanotti, O., 2016. High order ader schemes for a unified first order hyperbolic formulation of continuum mechanics: Viscous heat-conducting fluids and elastic solids. Journal of Computational Physics 314, 824–862.

Dumbser, M., Zanotti, O., 2009. Very high order pnpm schemes on unstructured meshes for the resistive relativistic mhd equations. Journal of Computational Physics 228, 6991 – 7006. URL: http://www.sciencedirect.com/science/article/pii/S0021999109003350, doi:https://doi.org/10.1016/j.jcp.2009.06.009.

Dumbser, M., Zanotti, O., Hidalgo, A., Balsara, D.S., 2013. Ader-weno finite volume schemes with space-time adaptive mesh refinement. Journal of Computational Physics 248, 257 – 286. URL: http://www.sciencedirect.com/science/article/pii/S0021999113002660, doi:https://doi.org/10.1016/j.jcp.2013.04.017.

Ern, A., Guermond, J., 2004. Theory and Practice of Finite Elements. Applied Mathematical Sciences, Springer New York. URL: https://books.google.it/books?id=CCjm79FbJbcC.

Ferrari, A., Dumbser, M., Toro, E.F., Armanini, A., 2009. A new 3d parallel sph scheme for free surface flows. Computers & Fluids 38, 1203 – 1217. URL: http://www.sciencedirect.com/science/article/pii/S0045793008002284, doi:10.1016/j.compfluid.2008.11.012.

Fourey, G., Hermange, C., Le Touzé, D., Oger, G., 2017. An efficient fsi coupling strategy between smoothed particle hydrodynamics and finite element methods. Computer Physics Communications 217, 66 – 81. URL: http://www.sciencedirect.com/science/article/pii/S0010465517301194, doi:https://doi.org/10.1016/j.cpc.2017.04.005.

Fourtakas, G., Dominguez, J.M., Vacondio, R., Rogers, B.D., 2019. Local uniform stencil (lust) boundary condition for arbitrary 3-d boundaries in parallel smoothed particle hydrodynamics (sph) models. Computers & Fluids 190, 346–361. URL: https://www.sciencedirect.com/science/article/pii/S0045793019301859, doi:https://doi.org/10.1016/j.compfluid.2019.06.009.

Gaburro, E., Boscheri, W., Chiocchetti, S., Klingenberg, C., Springel, V., Dumbser, M., 2020. High order direct Arbitrary-Lagrangian-Eulerian schemes on moving Voronoi meshes with topology changes. Journal of Computational Physics , 109167doi:10.1016/j.jcp.2019.109167.

Gingold, R.A., Monaghan, J.J., 1977. Smoothed particle hydrodynamics - Theory and application to non-spherical stars. Mon. Not. Roy. Astron. Soc. 181, 375–389. URL: http://adsabs.harvard.edu/cgi-bin/nph-bib_query?bibcode=1977MNRAS.181..375G.

Godunov, S., 1961. An interesting class of quasilinear systems. Dokl. Akad. Nauk SSSR 139(3), 521–523.

Godunov, S., Romenski, E., 1972. Nonstationary equations of the nonlinear theory of elasticity in Euler coordinates. Journal of Applied Mechanics and Technical Physics 13, 868–885.

Godunov, S., Romenski, E., 2003. Elements of Continuum Mechanics and Conservation Laws. Kluwer Academic/Plenum Publishers.

Godunov, S.K., 1959. Finite difference methods for the computation of discontinuous solutions of the equations of fluid dynamics. Mathematics of the USSR 47, 271–306.

Green, M.D., Vacondio, R., Peiró, J., 2019. A smoothed particle hydrodynamics numerical scheme with a consistent diffusion term for the continuity equation. Computers & Fluids 179, 632 – 644. URL: http://www.sciencedirect.com/science/article/pii/S0045793018309009, doi:https://doi.org/10.1016/j.compfluid.2018.11.020.

Gui-rong, L., Moubin, L., 2003. Smoothed Particle Hydrodynamics: A Meshfree Particle Method. World Scientific Publishing Company. URL: https://books.google.it/books?id=taPICgAAQBAJ.

Harten, A., Engquist, B., Osher, S., Chakravarthy, S., 1987. Uniformly high order accurate essentially non-oscillatory schemes III. Journal of Computational Physics 71, 231–303.

Idelsohn, S., Mier-Torrecilla, M., Oñate, E., 2009. Multi-fluid flows with the Particle Finite Element Method. Comput. Methods Appl. Mech. Engrg. 198, 2750–2767.

Idelsohn, S.R., Oñate, E., Pin, F.D., 2004. The Particle Finite Element Method: a powerful tool to solve incompressible flows with free-surfaces and breaking waves. International Journal for Numerical Methods in Engineering 61, 964–984.

Iwasaki, K., Inutsuka, S.i., 2011. Smoothed particle magnetohydrodynamics with a Riemann solver and the method of characteristics. Monthly Notices of the Royal Astronomical Society 418, 1668–1688. URL: https://doi.org/10.1111/j.1365-2966.2011.19588.x, doi:10.1111/j.1365-2966.2011.19588.x, arXiv:http://oup.prod.sis.lan/mnras/article-pdf/418/3/1668/18439664/mnras0418-1668.pdf.

Jiang, G.S., Shu, C.W., 1996. Efficient implementation of weighted eno schemes. Journal of Computational Physics 126, 202 -- 228. URL: http://www.sciencedirect.com/science/article/pii/S0021999196901308, doi:10.1006/jcph.1996.0130.

King, J., Lind, S., Nasar, A., 2020. High order difference schemes using the local anisotropic basis function method. Journal of Computational Physics 415, 109549. doi:https://doi.org/10.1016/j.jcp.2020.109549.

Kulasegaram, S., Bonet, J., Lewis, R.W., Profit, M., 2004. A variational formulation based contact algorithm for rigid boundaries in two-dimensional sph applications. Computational Mechanics 33, 316--325. doi:10.1007/s00466-003-0534-0.

Larese, A., Rossi, R., Oñate, E., Idelsohn, S., 2008. Validation of the Particle Finite Element Method (PFEM) for Simulation of the Free-Surface Flows. Engineering Computations 25, 385--425.

Levy, D., Puppo, G., Russo, G., 1999. Central WENO schemes for hyperbolic systems of conservation laws. M2AN Math. Model. Numer. Anal. 33, 547--571.

Levy, D., Puppo, G., Russo, G., 2000. Compact central WENO schemes for multidimensional conservation laws. SIAM J. Sci. Comput. 22, 656--672.

Lind, S., Stansby, P., 2016. High-order eulerian incompressible smoothed particle hydrodynamics with transition to lagrangian free-surface motion. Journal of Computational Physics 326, 290 -- 311. URL: http://www.sciencedirect.com/science/article/pii/S0021999116304041,

doi:https://doi.org/10.1016/j.jcp.2016.08.047.
Lind, S., Xu, R., Stansby, P., Rogers, B., 2012. Incompressible smoothed particle hydrodynamics for free-surface flows: A generalised diffusion-based algorithm for stability and validations for impulsive flows and propagating waves. Journal of Computational Physics 231, 1499 -- 1523. URL: http://www.sciencedirect.com/science/article/pii/S0021999111006279, doi:https://doi.org/10.1016/j.jcp.2011.10.027.
Liu, M., Liu, G., 2006. Restoring particle consistency in smoothed particle hydrodynamics. Applied Numerical Mathematics 56, 19 -- 36. URL: http://www.sciencedirect.com/science/article/pii/S0168927405000565, doi:https://doi.org/10.1016/j.apnum.2005.02.012.
Liu, W.K., Jun, S., Li, S., Adee, J., Belytschko, T., 1995. Reproducing kernel particle methods for structural dynamics. International Journal for Numerical Methods in Engineering 38, 1655--1679. URL: https://onlinelibrary.wiley.com/doi/abs/10.1002/nme.1620381005, doi:10.1002/nme.1620381005, arXiv:https://onlinelibrary.wiley.com/doi/pdf/10.1002/nme.1620381005.
Marongiu, J., Leboeuf, F., Caro, J., Parkinson, E., 2010. Free surface flows simulations in pelton turbines using an hybrid sph-ale method. Journal of Hydraulic Research 48, 40--49. URL: https://doi.org/10.1080/00221686.2010.9641244, doi:10.1080/00221686.2010.9641244, arXiv:https://doi.org/10.1080/00221686.2010.9641244.
Marrone, S., Antuono, M., Colagrossi, A., Colicchio, G., Touzé, D.L., Graziani, G., 2011. delta-sph model for simulating violent impact flows. Computer Methods in Applied Mechanics and Engineering 200, 1526 -- 1542. URL: http://www.sciencedirect.com/science/article/pii/S0045782510003725, doi:https://doi.org/10.1016/j.cma.2010.12.016.
McLoone, M., Quinlan, N.J., 2020. Particle transport velocity correction for the finite volume particle method for multi-resolution particle distributions and exact geometric boundaries. Engineering Analysis with Boundary Elements 114, 114 -- 126. URL: http://www.sciencedirect.com/science/article/pii/S0955799720300412, doi:https://doi.org/10.1016/j.enganabound.2020.02.003.
Molteni, D., Colagrossi, A., 2009. A simple procedure to improve the pressure evaluation in hydrodynamic context using the sph. Computer Physics Communications 180, 861 -- 872. URL: http://www.sciencedirect.com/science/article/pii/S0010465508004219, doi:https://doi.org/10.1016/j.cpc.2008.12.004.
Monaghan, J.J., 1994. Simulating free surface flows with sph. Journal of Computational Physics 110, 399--406. doi:10.1006/jcph.1994.1034.
Monaghan, J.J., 2005. Smoothed particle hydrodynamics. Reports on Progress in Physics 68, 1703. URL: http://stacks.iop.org/0034-4885/68/i=8/a=R01.
Nogueira, X., Ramírez, L., Clain, S., Loubère, R., Cueto-Felgueroso, L., Colominas, I., 2016. High-accurate sph method with multidimensional optimal order detection limiting. Computer Methods in Applied Mechanics and Engineering 310, 134 -- 155. URL: http://www.sciencedirect.com/science/article/pii/S0045782516306697, doi:https://doi.org/10.1016/j.cma.2016.06.032.
Oger, G., Marrone, S., Touzé, D.L., de Leffe, M., 2016a. Sph accuracy improvement through the combination of a quasi-lagrangian shifting transport velocity and consistent ale formalisms. Journal of Computational Physics 313, 76 -- 98. URL: http://www.sciencedirect.com/science/article/pii/S0021999116001030, doi:https://doi.org/10.1016/j.jcp.2016.02.039.
Oger, G., Marrone, S., Touzé], D.L., [de Leffe], M., 2016b. Sph accuracy improvement through the combination of a quasi-lagrangian shifting transport velocity and consistent ale formalisms. Journal of Computational Physics 313, 76 -- 98. URL: http://www.sciencedirect.com/science/article/pii/S0021999116001030, doi:https://doi.org/10.1016/j.jcp.2016.02.039.
Oger, G., Touzé, D.L., Guibert, D., de Leffe, M., Biddiscombe, J., Soumagne, J., Piccinali, J.G., 2016c. On distributed memory mpi-based parallelization of sph codes in massive hpc context. Computer Physics Communications 200, 1 -- 14. URL: http://www.sciencedirect.com/science/article/pii/S0010465515003070, doi:https://doi.org/10.1016/j.cpc.2015.08.021.
Oñate, E., Celigueta, M., Idelsohn, S., Salazar, F., Suarez, B., 2011. Possibilities of the Particle Finite Element Method for fluid-soil-structure interaction problems. Journal of Computational Mechanics 48, 307--318.
Oñate, E., Idelsohn, S., Celigueta, M., Rossi, R., 2008. Advances in the Particle Finite Element Method for the Analysis of Fluid-Multibody Interaction and Bed Erosion in Free-surface Flows. Computer Methods in Applied Mechanics and Engineering 197, 1777--1800.
Orszag, S.A., Tang, C.M., 1979. Small-scale structure of two-dimensional magnetohydrodynamic turbulence. Journal of Fluid Mechanics 90, 129--143. doi:10.1017/S002211207900210X.
Peshkov, I., Romenski, E., 2016. A hyperbolic model for viscous newtonian flows. Continuum Mechanics and Thermodynamics 28, 85--104.
Phoevos, K., Anagnostopoulos, J., Papantonis, E., 2012. An improved muscl treatment for the sph-ale method: comparison with the standard sph method for the jet impingement case. International Journal for Numerical Methods in Fluids 71, 1152--1177. URL: https://onlinelibrary.wiley.com/doi/abs/10.1002/fld.3706, doi:10.1002/fld.3706, arXiv:https://onlinelibrary.wiley.com/doi/pdf/10.1002/fld.3706.
Pin, F.D., Idelsohn, S.R., Oñate, E., Aubry, R., 2007. The ALE/Lagrangian Particle Finite Element Method: A new approach to computation of free-surface flows and fluid-object interactions. Computers and Fluids 36, 27--38.

Pourya, O., K., S.P., D., R.B., 2012. Wave body interaction in 2d using smoothed particle hydrodynamics (sph) with variable particle mass. International Journal for Numerical Methods in Fluids 68, 686--705. URL: https://onlinelibrary.wiley.com/doi/abs/10.1002/fld.2528, doi:10.1002/fld.2528, arXiv:https://onlinelibrary.wiley.com/doi/pdf/10.1002/fld.2528.

Pourya, O., K., S.P., D., R.B., 2013. Sph for 3d floating bodies using variable mass particle distribution. International Journal for Numerical Methods in Fluids 72, 427--452. URL: https://onlinelibrary.wiley.com/doi/abs/10.1002/fld.3749, doi:10.1002/fld.3749, arXiv:https://onlinelibrary.wiley.com/doi/pdf/10.1002/fld.3749.

Price, D.J., Wurster, J., Tricco, T.S., Nixon, C., Toupin, S., Pettitt, A., Chan, C., Mentiplay, D., Laibe, G., Glover, S., et al., 2018. Phantom: A smoothed particle hydrodynamics and magnetohydrodynamics code for astrophysics. Publications of the Astronomical Society of Australia 35, e031. doi:10.1017/pasa.2018.25.

Randles, P., Libersky, L., 1996. Smoothed particle hydrodynamics: Some recent improvements and applications. Computer Methods in Applied Mechanics and Engineering 139, 375 -- 408. URL: http://www.sciencedirect.com/science/article/pii/S0045782596010900, doi:https://doi.org/10.1016/S0045-7825(96)01090-0.

Rogers, B.D., Dalrymple, R.A., Stansby, P.K., 2010. Simulation of caisson breakwater movement using 2-d sph. Journal of Hydraulic Research 48, 135--141. URL: https://doi.org/10.1080/00221686.2010.9641254, doi:10.1080/00221686.2010.9641254, arXiv:https://doi.org/10.1080/00221686.2010.9641254.

Romenski, E., 1998. Hyperbolic systems of thermodynamically compatible conservation laws in continuum mechanics. Mathematical and computer modelling 28(10), 115--130.

Rossi, G., Dumbser, M., Armanini, A., 2017. A well-balanced path conservative SPH scheme for nonconservative hyperbolic systems with applications to shallow water and multi-phase flows. Computers and Fluids 154, 102--122.

Rusanov, V.V., 1961. Calculation of interaction of non--steady shock waves with obstacles. J. Comput. Math. Phys. USSR 1, 267--279.

Semplice, M., Coco, A., Russo, G., 2016. Adaptive mesh refinement for hyperbolic systems based on third-order compact WENO reconstruction. Journal of Scientific Computing 66, 692--724.

Sibilla, S., 2015. An algorithm to improve consistency in smoothed particle hydrodynamics. Computers & Fluids 118, 148 -- 158. URL: http://www.sciencedirect.com/science/article/pii/S0045793015001954, doi:https://doi.org/10.1016/j.compfluid.2015.06.012.

Sod, G., 1978. Survey of several finite difference methods for systems of nonlinear hyperbolic conservation laws. Journal Name: J. Comput. Phys. URL: http://www.osti.gov/scitech/servlets/purl/6812922.

Springel, V., 2010. E pur si muove: Galilean-invariant cosmological hydrodynamical simulations on a moving mesh. Monthly Notices of the Royal Astronomical Society (MNRAS) 401, 791--851.

Sun, P., Colagrossi, A., Marrone, S., Zhang, A., 2017. The delta plus-sph model: Simple procedures for a further improvement of the sph scheme. Computer Methods in Applied Mechanics and Engineering 315, 25 -- 49. URL: http://www.sciencedirect.com/science/article/pii/S0045782516309112, doi:https://doi.org/10.1016/j.cma.2016.10.028.

Titarev, V., Toro, E., 2002. ADER: Arbitrary high order Godunov approach. Journal of Scientific Computing 17, 609--618.

Titarev, V., Toro, E., 2005. ADER schemes for three-dimensional nonlinear hyperbolic systems. Journal of Computational Physics 204, 715--736.

Toro, E., 1997. Riemann solvers and numerical methods for fluid dynamics: a practical introduction. Springer. URL: http://books.google.cl/books?id=6QFAAQAAIAAJ.

Toro, E., Titarev, V., 2002. Solution of the generalized Riemann problem for advection-reaction equations. Proc. Roy. Soc. London 458, 271--281.

Toro, E.F., Titarev, V.A., 2006. Derivative Riemann solvers for systems of conservation laws and ADER methods. Journal of Computational Physics 212, 150--165.

Tricco, T.S., Price, D.J., Bate, M.R., 2016. Constrained hyperbolic divergence cleaning in smoothed particle magnetohydrodynamics with variable cleaning speeds. Journal of Computational Physics 322, 326 -- 344. URL: http://www.sciencedirect.com/science/article/pii/S0021999116302789, doi:https://doi.org/10.1016/j.jcp.2016.06.053.

van Leer, B., 1979. Towards the ultimate conservative difference scheme V: A second order sequel to Godunov's method. Journal of Computational Physics 32, 101--136.

Vila, J.P., 1999. On particle weighted methods and smooth particle hydrodynamics. Mathematical Models and Methods in Applied Sciences 09, 161--209. doi:10.1142/S0218202599000117.

Violeau, D., Fonty, T., 2019. Calculating the smoothing error in sph. Computers & Fluids 191, 104240. URL: http://www.sciencedirect.com/science/article/pii/S0045793019302026, doi:https://doi.org/10.1016/j.compfluid.2019.104240.

Xu, R., Stansby, P., Laurence, D., 2009. Accuracy and stability in incompressible sph (isph) based on the projection method and a new approach. Journal of Computational Physics 228, 6703 -- 6725. URL: http://www.sciencedirect.com/science/article/pii/S0021999109002885, doi:https://doi.org/10.1016/j.jcp.2009.05.032.

Zanotti, O., Fambri, F., Dumbser, M., Hidalgo, A., 2015. Space-time adaptive ader discontinuous galerkin finite element schemes with a posteriori sub-cell finite volume limiting. Computers & Fluids 118, 204 -- 224. URL: http://www.sciencedirect.com/science/article/pii/S0045793015002030,

doi:https://doi.org/10.1016/j.compfluid.2015.06.020.

Zwillinger, D., 2003. CRC Standard Mathematical Tables and Formulae: Editor-in-chief, Daniel Zwillinger. CRC Standard Mathematical Tables and Formulae, Taylor & Francis Group. URL: http://books.google.cl/books?id=9zXt1yFQE2UC.